

# Pinpointing the mechanism of magnetic enhancement in modern soils using high-resolution magnetic field imaging

Roger R Fu<sup>1</sup>, Barbara A. Maher<sup>2</sup>, Junsheng Nie<sup>3</sup>, Peng Gao<sup>3</sup>, Thomas Berndt<sup>4</sup>, Elizabeth Folsom<sup>1</sup>, and Timothy Cavanaugh<sup>1</sup>

<sup>1</sup>Harvard University

<sup>2</sup>Lancaster University

<sup>3</sup>Lanzhou University

<sup>4</sup>Peking University

December 21, 2022

## Abstract

In well-buffered modern soils, higher annual rainfall is associated with enhanced soil ferrimagnetic mineral content, especially of ultrafine particles that result in distinctive observable rock magnetic properties. Hence, paleosol magnetism has been widely used as a paleoprecipitation proxy. Identifying the dominant mechanism(s) of magnetic enhancement in a given sample is critical for reliable inference of paleoprecipitation. Here we use high-resolution magnetic field and electron microscopy to identify the grain-scale setting and formation pathway of magnetic enhancement in two modern soils developed in higher ( $\sim 580$  mm/y) and lower ( $\sim 190$  mm/y) precipitation settings from the Qilianshan Range, China. We find both soils contain 1-30  $\mu\text{m}$  aeolian Fe-oxide grains with indistinguishable rock magnetic properties while the higher-precipitation soil contains an additional population of ultrafine ( $< 150$  nm), magnetically distinct magnetite grains. We show that the in situ precipitation of these ultrafine particles, likely during wet-dry cycling, is the only significant magnetic enhancement mechanism in this soil. These results demonstrate the potential for quantum diamond microscope (QDM) magnetic microscopy to extract magnetic information from distinct, even intimately mixed, grain populations. This information can be used to evaluate the contribution of distinct enhancement mechanisms to the total magnetization.

# Pinpointing the mechanism of magnetic enhancement in modern soils using high-resolution magnetic field imaging

Roger R. Fu<sup>1</sup>, Barbara A. Maher<sup>2</sup>, Junsheng Nie<sup>3</sup>, Peng Gao<sup>3</sup>, Thomas Berndt<sup>4</sup>, Elizabeth Folsom<sup>1</sup>, Timothy Cavanaugh<sup>5</sup>

<sup>1</sup>Department of Earth and Planetary Sciences, Harvard University, Cambridge, Massachusetts, USA.

<sup>2</sup>Centre for Environmental Magnetism and Palaeomagnetism, Lancaster Environment Centre, University of Lancaster, Lancaster, United Kingdom

<sup>3</sup>Key Laboratory of Western China's Environment System (Ministry of Education), College of Earth and Environmental Sciences, Lanzhou University, Lanzhou, China

<sup>4</sup>Department of Geophysics, School of Earth and Space Sciences, Peking University, Beijing, China

<sup>5</sup>Center for Nanoscale Systems, Harvard University, Cambridge, Massachusetts, USA.

## Abstract

In well-buffered modern soils, higher annual rainfall is associated with enhanced soil ferrimagnetic mineral content, especially of ultrafine particles that result in distinctive observable rock magnetic properties. Hence, paleosol magnetism has been widely used as a paleoprecipitation proxy. Identifying the dominant mechanism(s) of magnetic enhancement in a given sample is critical for reliable inference of paleoprecipitation. Here we use high-resolution magnetic field and electron microscopy to identify the grain-scale setting and formation pathway of magnetic enhancement in two modern soils developed in higher (~580 mm/y) and lower (~190 mm/y) precipitation settings from the Qilianshan Range, China. We find both soils contain 1-30  $\mu\text{m}$  aeolian Fe-oxide grains with indistinguishable rock magnetic properties while the higher-precipitation soil contains an additional population of ultrafine (<150 nm), magnetically distinct magnetite grains. We show that the *in situ* precipitation of these ultrafine particles, likely during wet-dry cycling, is the only significant magnetic enhancement mechanism in this soil. These results demonstrate the potential for quantum diamond microscope (QDM) magnetic microscopy to extract magnetic information from distinct, even intimately mixed, grain populations. This information can be used to evaluate the contribution of distinct enhancement mechanisms to the total magnetization.

## Plain Language Summary

Reconstructing how natural climate variations in the past influenced rainfall patterns is important for understanding how rainfall would respond to our currently changing climate. The amount and properties of microscopic, magnetic minerals in soil can change due to interactions with pore water; therefore, characterizing the magnetic properties of soils can aid in quantifying past rainfall. We use the quantum diamond microscope

(QDM) a device that allows micrometer-scale mapping of magnetic sources in rock and soil samples, to investigate the magnetic properties of two soils formed in low- and high-rainfall environments. We find that, although both soils contain wind-blown, magnetic dust, only the high-rainfall soil contains an abundant, highly magnetic population of magnetite grains formed in soil pore spaces during repeated cycles of wetting and drying. These observations demonstrate the dominant pathway by which soil magnetism responds to rainfall and showcase the ability of QDM mapping to reliably identify the mechanism of magnetism modification in soils.

## Introduction

The challenge of understanding how patterns of rainfall will respond to a changing climate has motivated the study of ancient precipitation during times of natural climate variability (Shepherd, 2014; McGee, 2020). Paleosols developed in and interbedded with continental-scale loess deposits represent a proxy for ancient precipitation regimes. In particular, the Chinese Loess Plateau (CLP) has been the subject of focused investigation due to its unique record comprising ~350 m of sediments deposited quasi-continuously over the past >2.6 million years (My) (Maher, 2016). Robust correlations between the magnetic susceptibility of CLP deposits, Milankovitch cyclicity, and established archives such as the marine benthic  $\delta^{18}\text{O}$  record have demonstrated that paleoclimate information is encoded in the magnetism of CLP sediments (Heller and Liu, 1984; Maher and Thompson, 1992; Sun et al., 2006; Nie et al., 2008; Maher, 2016).

Understanding the paleoclimatic implications of the CLP magnetism record requires identification of the physical condition or conditions that lead to magnetic enhancement. Early studies hypothesized that preferential soil compaction during wet intervals or variations in non-magnetic dust deposition rates can explain the link between hydrological environment and magnetism (Heller and Liu, 1986; Kukla et al., 1988).

Subsequent studies have discovered and quantified distinct coarse ( $\geq 2 \mu\text{m}$  diameter) and ultrafine ( $\leq 100 \text{ nm}$ ) populations of ferrimagnetic grains in CLP paleosols (Maher and Thompson, 1991, 1992). Similarities between the paleosol ultrafine population and magnetite particles formed in laboratory reactions under soil-like conditions have led to the now widely accepted model that magnetically enriched intervals in the CLP frequently represent times of enhanced rainfall, which led to enhanced redox activity and *in situ* formation of the ultrafine ferrimagnetic grains (Maher and Taylor, 1988).

Multiple physical models have been proposed for the formation of ultrafine ferrimagnetic particles. Based on a comparison of soils from a range of climatic conditions and laboratory synthesis experiments (Maher and Taylor, 1988), Maher (1998) proposed that repeated wetting and drying cycles can lead to the precipitation of ultrafine magnetite, likely aided by  $\text{Fe}^{3+}$ -reducing bacteria, while simultaneously preventing wholesale oxidation of these ultrafine products into weakly magnetic  $\text{Fe}^{3+}$  phases such as goethite and hematite. High-resolution electron microscopy suggests that magnetite,

rather than maghemite, dominates the mineralogy of the ultrafine pedogenic ferrimagnets (Ahmed and Maher, 2018). Quantitative modeling of this process and comparison to the magnetism-rainfall relationship, or climofunction, of modern soils appear to support its occurrence across a wide range of rainfall regimes up to ~1000 mm y<sup>-1</sup> (Maher et al., 2003; Geiss et al., 2008; Orgeira et al., 2011; Balsam et al., 2011). According to this model, pedogenic magnetic content in ancient deposits such as those of the CLP is a quantitative indicator of rainfall amount (Maher and Possolo, 2013), modified in some locations by soil water changes due to evapotranspiration (Orgeira et al., 2011).

Other authors, however, have attributed enrichment of ultrafine ferrimagnets to direct oxidation of aeolian Fe-oxides or concentration of preexisting silicate-hosted Fe-oxide particles. Maghemite found in association with coarser aeolian magnetite provides evidence for ultrafine maghemite production from magnetite oxidation, although the proportional contribution of this pathway to total soil magnetic enhancement is unclear (Chen et al., 2005). Meanwhile, scanning electron microscopy (SEM) observations of CLP paleosols have revealed higher abundance of coarse (>10 µm) silicate minerals containing abundant <100 nm scale ferrimagnets in soils with strongest magnetic enhancement (Yang et al., 2013). Although ferrimagnetic grain formation via these pathways may also depend on local climate, additional factors such as the concentration of magnetite and Fe-bearing silicates in the unmodified aeolian source are also suggested to play a role.

A final proposed pathway for forming pedogenic ferrimagnets involves the transformation of ferrihydrite to single domain maghemite, rather than magnetite, and ultimately to hematite without a role for wetting and drying cycles and the accompanying reducing conditions. Correlations between the concentration of ultrafine ferrimagnets and hematite in natural soils and observed growth of similar-sized maghemite in laboratory experiments have provided support for this mechanism (Torrent et al., 2006, 2007; Liu et al., 2008). If validated, this origin for soil magnetic enhancement implies that higher ferrimagnetic content is an indicator for warmer temperatures, which favors the transformation of Fe<sup>3+</sup> in ferrihydrite into maghemite and hematite instead of into weakly magnetic goethite.

In summary, different mechanisms of magnetic enhancement may be dominant depending on the specific soil composition and environment. Because these models predict distinct relationships between magnetic enhancement and climatic conditions, the dominant mechanism of magnetic enhancement in an ancient sample must be identified before paleoclimatic inferences can be made.

As a further complication, multiple enhancement mechanisms with distinct relationships to rainfall may act simultaneously on the same sample. For example, the provenance of aeolian grains to the CLP varied significantly in both time and space (Xiao et al., 2012; Zhang et al., 2021). Hence, even if a similar process of *in situ* magnetic grain growth process occurred in multiple samples, their magnetic properties and the degree

of authigenic enhancement may depend on the composition of aeolian precursors as well as the degree of rainfall-induced enhancement.

Detailed microscopy of modern and ancient soils may aid in identifying the mechanism(s) of magnetic enhancement. Identification of ferrimagnetic grains co-occurring with, for example, detrital Fe-oxides or Fe-bearing silicates may provide evidence for their formation from these precursors. In parallel, crystallographic and compositional studies can distinguish between magnetite and maghemite along with the concentration of substitutional trace elements. For example, lattice-scale observations of soil ferrimagnets have identified Al-poor magnetite as the main contributor to magnetism in a modern soil from the UK and some CLP paleosols (Ahmed and Maher, 2018). This observation appears inconsistent with the ferrihydrite → maghemite → hematite pathway described above, which produces Fe-oxides with several atomic percent Al<sup>3+</sup> substitution (Hu et al., 2013).

In this work, we use the quantum diamond microscope (QDM), a recently developed high-resolution magnetic field imager, to aid in understanding the mechanism of magnetic enhancement in modern soils from the Qilianshan Range, China, that developed in high-rainfall/low-temperature and low-rainfall/high-temperature settings. First, we use the high spatial resolution of the QDM to distinguish populations of ferrimagnetic grains within the soils and obtain magnetic information from each sub-population. We use this grain-scale magnetic characterization to constrain the physical location and chemical pathway of magnetic enhancement. Second, we use QDM maps to localize regions with high concentrations of magnetic sources to guide electron microscopy-based analyses of ferrimagnetic grains, thereby directly linking the source of magnetism to detailed analyses of grain composition.

## **Samples and Methods**

We collected A horizon soil samples between 5 and 10 cm depth from a transect in the Qilianshan Range representing a range of elevations to study how local temperature and rainfall correlate with differences in magnetic properties (Gao et al., 2021). These soils were developed in loessic parent material on the northern flank of the Qilianshan Range, which receives predominantly summer precipitation. The highest and lowest elevation samples were collected from 3533 m (101.85° E, 37.56° N) and 1859 m (102.3° E, 37.94° N) above sea level (Fig. S11 in Gao et al., 2021). The annual mean precipitation at these two sites is, respectively, 576.6 and 192.8 mm based on linear interpolation and extrapolation of annual mean precipitation data obtained between 2011 and 2020 from four meteorological stations at elevations of 2060 m (242.6 mm), 2710 m (403.9 mm), 3070 m (523.3mm), and 3600 m (584.3 mm) above sea level of the Qilianshan Range. The annual mean and summer mean air temperatures at the high-elevation, higher-precipitation site over the same period are -2.0°C and 6.9°C while those for the low-elevation, low-precipitation site are 9.6°C and 21.4°C.

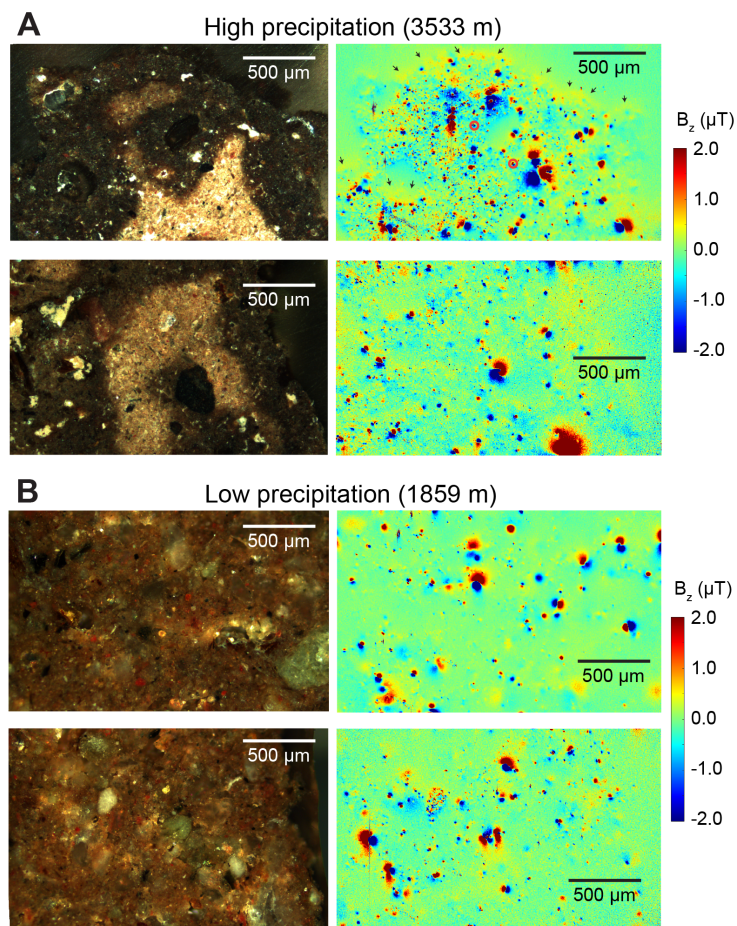


**Figure 1.** Representative QDM magnetic field maps of (A) high-elevation, high-rainfall, low-temperature and (B) low-elevation, low-rainfall, high-temperature modern soils. Photomicrographs in the left column were taken in reflected light with crossed polars. Positive (negative) values denote magnetic fields oriented out of (into) the page. All samples carry an ARM with bias field in the 12 o'clock direction. Note the diffuse positive magnetic fields at the 12 o'clock edge of the sample visible in the topmost QDM map (small black arrows). These fringing fields indicate the presence of an unresolved, fine grain population carrying a uniform magnetization. The two sources in red circles in panel (A) were further analyzed using electron microscopy in Fig. 6.

Once the dry soil samples arrived in the in the Harvard Paleomagnetism Lab, we first vacuum impregnated approximately 40 mm<sup>3</sup> volume of each using Epo-tek® 301 epoxy. The absence of detectable magnetic field signal outside the soil regions in QDM maps demonstrates the magnetic cleanness of the epoxy (Fig. 1). We then cut and polished a ~300  $\mu\text{m}$  thick section for each sample. We performed QDM magnetic field imaging in

projected magnetic microscopy (PMM) mode in a 0.9 mT bias magnetic field that was reversed during data acquisition, resulting in a 700 nT uncanceled field (Glenn et al., 2017). Most QDM magnetic field maps were integrated over ~30 minutes. The raw QDM data were then processed using GPU microwave spectra fitting routines in the *QDMLab* software package with a global fluorescence factor of 0.25 (Fu et al., 2020; Volk et al., 2022). Prior to the QDM experiments, we applied anhysteretic remanent magnetizations (ARM), isothermal remanent magnetizations (IRM), and alternating field (AF) demagnetization to the samples using the AC and DC coils on a 2G Enterprises model 755 superconducting rock magnetometer with installed RAPID system in the Harvard Paleomagnetism Lab. Bulk measurements of 5-10 mm sized blocks of the same soil samples were conducted with the same 2G Enterprises magnetometer. All data used in this study are available on the Harvard Dataverse (Fu et al., 2022).

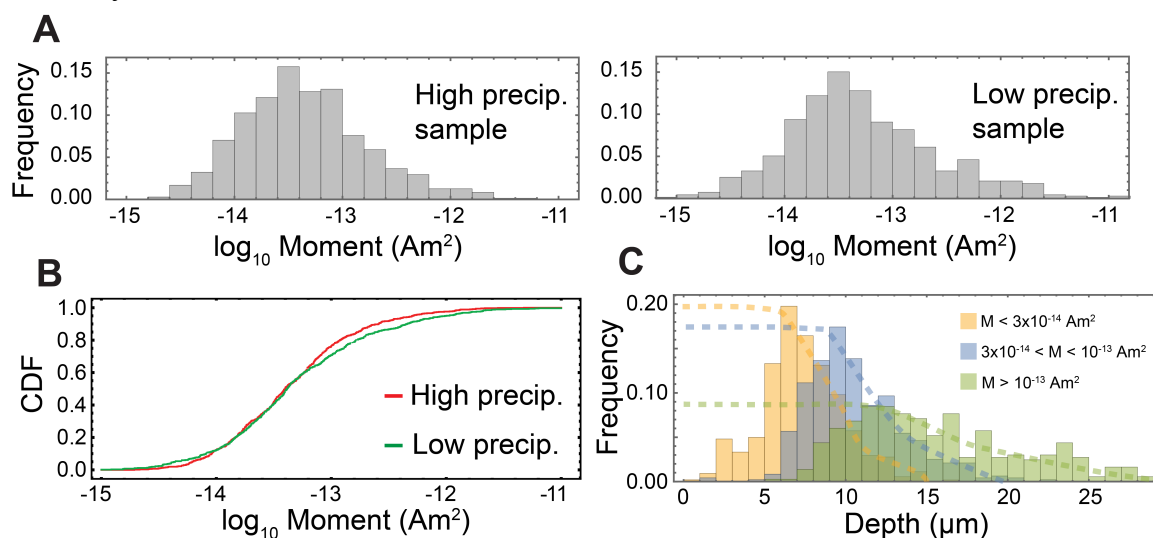


**Figure 2.** Single grain magnetizations for the coarse, individually resolved population of ferrimagnetic grains. (A) Distribution of magnetic moments for grains from the high- and low-precipitation samples. (B) Comparison of single grain magnetization distributions in the two soils displayed as a cumulative distribution function (CDF). A two-sample Kolmogorov-Smirnov test yields a  $p$  value of 0.13, implying insufficient evidence to demonstrate that the two populations have distinct distributions. (C) Distribution of depths of individual fitted sources separated by individual magnetic moments.

For QDM-based ARM experiments, we used a relatively high, 0.3 mT DC bias field to maximize the signal-to-noise ratio of magnet field maps. To quantify non-linearity in ARM acquisition, we imparted ARMs to bulk samples in 0.05 to 0.3 mT bias fields, finding that ARM intensities in a 0.3 mT bias field are 16% lower than expected from a linear extrapolation of lower bias field ARMs. We used this value to find the expected low-field ARM intensities before computing the ARM susceptibility. ARM bias fields and pulsed fields used in IRM acquisition were oriented to within  $2^\circ$  of the 12 o'clock, in-plane direction in all QDM maps.

After completing magnetic field imaging experiments, we carbon coated selected polished sections for analysis on a JEOL 7900F electron microscope at the Center for Nanoscale Systems at Harvard University. We used the backscattered electron (BSE) and Oxford Instruments energy dispersive spectroscopy (EDS) x-ray detectors to conduct high-resolution electron microscopy and elemental composition analysis. EDS data were quantified using Oxford Aztec software while quantification was performed using certified microanalysis standards for the measured elements and calibrated for the 5 keV beam energy.

## Results

### *Magnetic imaging of coarse magnetic population*

All QDM maps of ARM in the high and low-precipitation soils reveal abundant discrete remanence-carrying sources distributed throughout the sample volume (Fig. 1). We refer to these individually-resolved sources as the “coarse population” based on the high magnitude of individual magnetizations and electron microscopy showing them to be typically larger than several micrometers (see *Electron microscopy* Section below). To quantify the magnetization of each imaged grain, we fitted all isolated sources using a dipole model (Lima and Weiss, 2016; Fu et al., 2020), resulting in 672 and 711 fitted magnetic sources over a combined area of 57 and 41 mm<sup>2</sup> for the high- and low-precipitation samples, respectively. For both soils, the magnetic moment of individual coarse sources ranged between 10<sup>-15</sup> and 10<sup>-11</sup> Am<sup>2</sup> with a peak at approximately 3×10<sup>-14</sup> Am<sup>2</sup> (Fig. 2A).

To quantify the contribution of coarse sources to the total magnetization, we vector-summed the individual magnetizations and divided by the area and typical source depth, which is approximately 10 μm based on averaging the distribution of depths determined by net moment inversion (Fig. 2C). Sources at greater depths are progressively rarer due to the fall-off of their magnetic fields with distance. This analysis shows that the coarse magnetic sources contribute 4.5% and 40.6% of the bulk ARM for the high- and low-precipitation soils, respectively.

These percentages may underestimate the total coarse grain magnetization for several reasons. First, we binned pixels in 4×4 blocks to maximize signal-to-noise ratio for these ARM maps, resulting in a spatial resolution of 4.7 μm per pixel. Therefore, sources located fewer than a few μm from the surface would generate opposing magnetic fields that fall predominantly into a single pixel, preventing their identification. This effect produces the lack of fitted sources of any magnitude with less than ~3 μm depth (Fig. 2C). Second, because we only performed quantitative inversions on well-defined magnetic field signals, we excluded sources located in close proximity to neighboring ferrimagnetic particles, which results in highly non-dipolar magnetic field signatures (Fig. 1). This interference is more significant for stronger grains, which generate substantial magnetic field signal over a large volume and are therefore more likely to

interfere with neighboring sources. This effect accounts for the deficit of shallow and strongly magnetized grains among the sources in our compilation (Fig. 2C).

Regardless of the cause(s) of under-sampling, no physical mechanism can result in a true depletion of magnetic sources in the near surface given our randomly selected cut plane. We therefore estimate the contribution of missing shallow coarse magnetic sources by extrapolating the peak value of the depth histogram to the surface (dashed curves in Fig. 2C). This peak value is likely the best estimate for the true density of magnetic sources at a given depth, since recovered source concentrations are suppressed by magnetic field fall-off and by the near surface biases described above, respectively.

By this estimation, these missing sources appears to account for slightly over 50% of the total coarse source moment, implying that approximately 95% of the bulk magnetization in the low-precipitation soil can be attributed to coarse ferrimagnetic grains. This extrapolation is consistent with the lack of any other magnetic grain population, such as ultrafine particles (see below), observed in the low-precipitation soil. More advanced inversion techniques, including potential coupling to tomographic grain mapping (de Groot et al., 2021), can potentially result in the direct characterization of closer to 100% of resolvable magnetic sources in QDM maps.

Even without a complete inventory, the grain-level magnetization data on the coarse grains can be used to constrain their origin. Adopting a magnetite or maghemite composition, based on our electron microscopy results (see below), yields a diameter of 0.4, 1.0, and 10  $\mu\text{m}$  for weakly magnetized, modal, and strongly magnetized grains in this population assuming a saturation remanent magnetization to saturation magnetization ratio ( $M_{rs}/M_s$ ) of between 0.2 and 0.02 corresponding to the appropriate grain size (Roberts et al., 2017). These grain sizes are much larger than those reported for pedogenic and biogenic magnetite populations (Maher and Thompson, 1992; Nie et al., 2010). In fact, our electron microscopy of coarse grains (see below) shows that some grains associated with coarse magnetic signals are even larger, with diameters in the 10-30  $\mu\text{m}$  range. The  $\leq 10$   $\mu\text{m}$  equivalent diameter estimated from grain magnetizations may therefore represent ferrimagnetic sub-regions within the polymineralic grains. These 0.4 - 30  $\mu\text{m}$  ferrimagnet grain sizes are on the finer end of, but still overlap significantly with, those of other wind-blown loess deposits, which are dominated by 10-100  $\mu\text{m}$  diameter particles (Újvári et al., 2016). We therefore conclude that the discrete ferrimagnetic sources observed in both high- and low-precipitation soil samples are associated with the aeolian supply of coarse detrital magnetic grains.

We observe no significant difference between the distribution of the coarse population magnetic moment magnitudes of the low- and high-rainfall soils using a two sample Kolmogorov-Smirnov test ( $p = 0.13$ ; Fig. 2B). Further, the total magnetic moment of all resolved grains in each 3.15  $\text{mm}^2$  field of view is  $9.45 \pm 6.85 \times 10^{-12} \text{ Am}^2$  and  $6.82 \pm 2.68 \times 10^{-12} \text{ Am}^2$  ( $1\sigma$ ) for the high- and low-precipitation soils, respectively, again implying no resolvable difference between the two sites (Student's t-test  $p = 0.20$ ). Together, these

data demonstrate that the grain-level properties and the concentration of coarse-grained magnetic sources are indistinguishable at these high- and low-precipitation sites. This suggests that the coarse sources in both samples share the same detrital origin and that no additional magnetic enhancement occurred for this grain population at the higher rainfall locality.

#### *Magnetic imaging of ultrafine magnetic population in high-precipitation sample*

In contrast to the low-precipitation soil, the high-precipitation soil contains an additional population of unresolved, high-ARM susceptibility ( $k_{ARM}$ ) ferrimagnetic grains in addition to the above-described coarse ferrimagnetic grains. We hereafter referred to these grains as the “ultrafine” population. Although individual magnetic grains in this population are not resolvable in either QDM or optical images, diffuse positive and negative magnetic fields at the 12 o’clock and 6 o’clock edge of the sample are visible in the QDM maps for this high-precipitation soil (Fig. 1A, small black arrows). This magnetic field morphology indicates a net magnetization in the 12 o’clock direction, implying that the sample volume has acquired an ARM in the direction of the bias field. The consistent intensity of these fringing fields along the entire sample edge attests to the nearly uniform presence of this unresolved magnetic grain population throughout the volume of the high-precipitation soil. Notably, these fringing fields are not observed in the low-precipitation soil maps (Fig. 1B), implying that this ultrafine grain population is not measurably present in those samples.

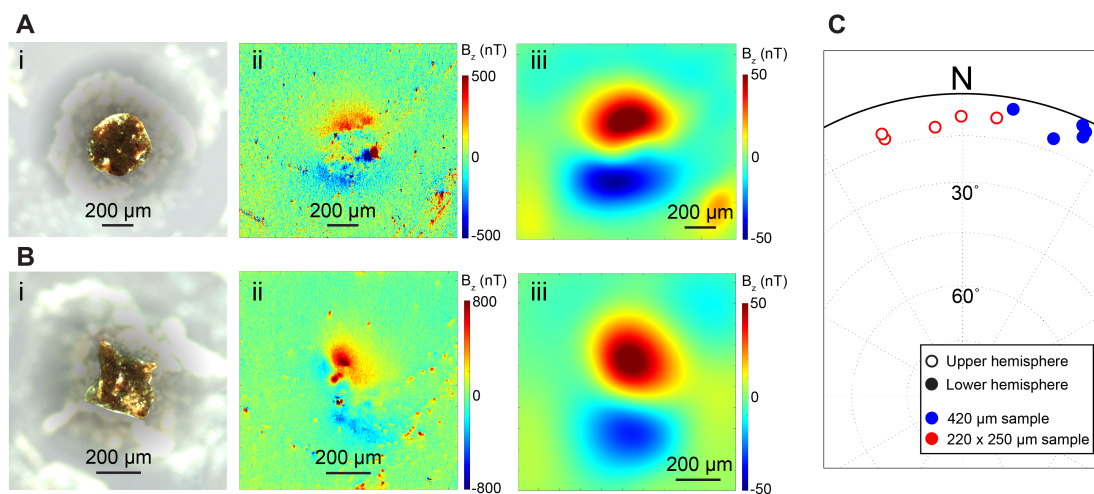


**Figure 3.** Net magnetic moment analysis of high-precipitation soil sub-volumes dominated by ultrafine grained magnetic carriers. Panels i through iii show, respectively, a reflected light, crossed polars photomicrograph, a raw QDM magnetic field map, and upward-continued and coarse source-subtracted magnetic field maps of the (A) 420  $\mu\text{m}$ -diameter and (B) 220 $\times$ 250  $\mu\text{m}$  sub-volumes. (C) Equal area stereonet projection of repeat ARM directions recovered from the two ultra-fine grain dominated sub-volumes. Bias field direction for all ARMs is due north with zero inclination.

We can use the QDM data to characterize the concentration, coercivity spectrum, and grain size distribution of this ultrafine ferrimagnetic grain population. We first used non-magnetic tools to isolate a 300  $\mu\text{m}$  thick, 420  $\mu\text{m}$ -diameter sub-volume of the high-precipitation sample relatively free from coarse magnetic sources (Fig. 3). We refer to this specimen hereafter as the “ultrafine grain sub-volume”. Next, we imparted a 300 mT AC field and 0.3 mT DC field ARM followed by stepwise AF demagnetization in 2.5 to 5 mT steps up to 40 mT, by which point the direction of magnetization was fully randomized. We subtracted the fitted dipole signal arising from a coarse magnetic particle and fitted for the net magnetic moment of the remaining signal after 120  $\mu\text{m}$  upward continuation using a dipole model after each ARM or AF application (Fu et al., 2020). Further, we measured the magnetization of this sub-volume after imparting a 0.3 T IRM. As evidenced by the AF demagnetization sequence (Fig. 4), the soft coercivity of the ultrafine grain sub-volume implies that this low DC field value is able to produce a near-saturation IRM.

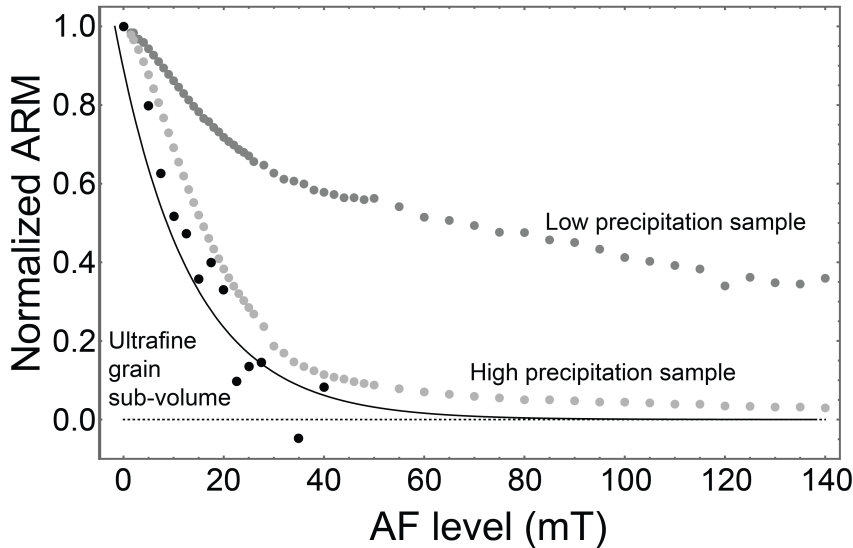


**Figure 4.** AF demagnetization of ARM for high- and low-precipitation bulk samples and the ultrafine grain sub-volume. Black solid line shows the best-fit exponential curve for the ultrafine grain sub-volume data. Plotted magnetization is the projection of the measured vector magnetization in the ARM bias field direction.

We first quantify the contribution of the ultrafine ferrimagnetic grain population to the total magnetization. By normalizing the ultrafine sub-volume ARM moment to its volume and comparing it to the ARM intensity of the bulk sample, we find that the ultrafine population can account for  $88 \pm 8\%$  ( $1\sigma$ ) of the total sample ARM, where the uncertainty is based on the reproducibility of the ARM.

Combining this value with the 4.5% of ARM contributed by the coarse grain population in the high-precipitation sample results in  $\sim 93\%$  of the measured bulk

magnetization. Adopting the low-precipitation sample as a guide, individually quantifiable coarse grain magnetic sources account for 40% of the total magnetization while the remaining 60% likely arises from additional coarse grain sources that could not be sufficiently isolated (see discussion above). Therefore, the total contribution of coarse grains in the high-precipitation soil is likely  $\sim 11\%$ , bringing the ultrafine plus coarse grain magnetization in the high-precipitation soil very close to 100%. This consistency both indicates that no other significant ferrimagnetic grain population is present in the high-precipitation soil and corroborates the estimated 40:60 ratio of individually quantified to not individually quantified coarse grain sources estimated above.

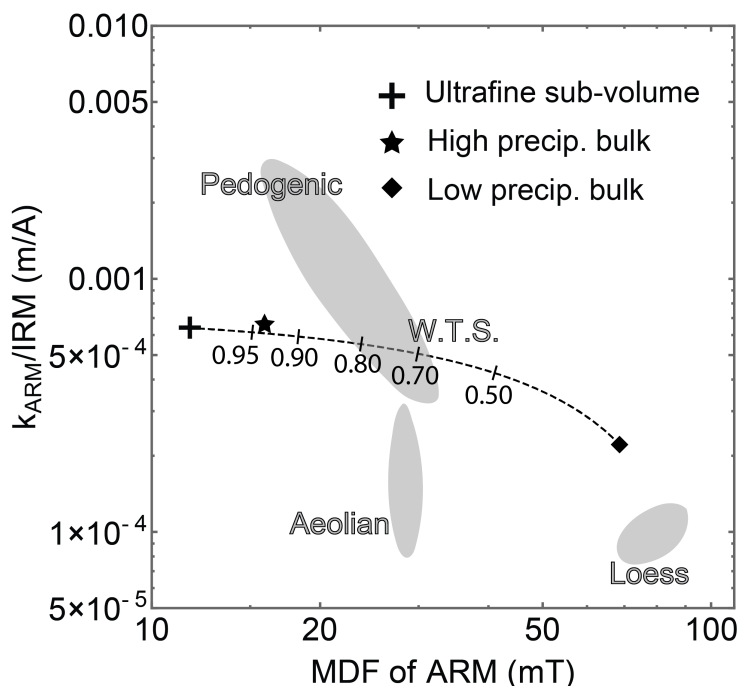


**Figure 5.** Coercivity and IRM-normalized ARM susceptibility of the ultrafine sub-volume and of the high- and low-precipitation bulk soils. Dashed curve indicates a linear mixing curve between the ultrafine and low-precipitation bulk endmembers with the number indicating volume fraction of the ultrafine grain population. Gray regions and labels are from compilation study by Egli (2004). W.T.S. denotes water transported sediments, including fluvial and proglacial environments.

Second, we characterized the magnetic properties of the ultrafine population using a combination of ARM demagnetization and IRM acquisition. Using QDM data from the  $420\ \mu\text{m}$ -diameter ultrafine grain sub-volume, we computed the IRM-normalized ARM susceptibility ( $k_{ARM}/IRM$ ) and mean destructive field of ARM ( $MDF$ ; Fig. 4). Together, these two parameters are a well-studied, albeit non-unique, proxy for magnetite grain size and origin with ultrafine fine, pedogenic magnetites typically showing high  $k_{ARM}$

and low  $MDF$  (Maher, 1988; Egli, 2004). Our analyses show that the ultrafine ferrimagnetic grains fall near the region encompassed by pedogenic magnetite, although with lower ARM susceptibility ( $\frac{k_{ARM}}{IRM} = 6.4 \times 10^{-4} \text{ m A}^{-1}$ ;  $MDF_{ARM} = 11.7 \text{ mT}$ ; Fig. 5). For comparison, the high-precipitation bulk soil sample revealed moderately higher coercivity and similar ARM susceptibility, although still corresponding to pedogenic magnetite ( $\frac{k_{ARM}}{IRM} = 6.7 \times 10^{-4} \text{ m A}^{-1}$ ;  $MDF_{ARM} = 15.9 \text{ mT}$ ).

As presented earlier, the analysis of ARM intensities contributed by the ultrafine and coarse grain populations within the high-precipitation soil implies that the bulk  $k_{ARM}/IRM$  and  $MDF_{ARM}$  parameters should represent a linear combination of ultrafine and coarse grain signal with the former population dominating. A bulk sample from the low-precipitation locality, which appears to contain only coarse grain-hosted magnetization in QDM maps, displays magnetic properties corresponding to a typical, weakly magnetized, highly oxidized loess deposit ( $\frac{k_{ARM}}{IRM} = 2.2 \times 10^{-4} \text{ m A}^{-1}$ ;  $MDF_{ARM} = 68.7 \text{ mT}$ ; Fig. 5). Adopting these properties for the coarse-grained endmember, a linear mixing model shows that the bulk  $k_{ARM}/IRM$  and  $MDF_{ARM}$  of the high-precipitation sample is best explained by a 94% to 6% mixture of ultrafine and coarse grain components by volume, respectively. This proportion is within uncertainty of the  $88 \pm 8\%$  by volume estimate derived earlier from ARM intensity and confirms that the magnetization of the high-precipitation sample is dominated by the ultrafine grain population.

In summary, these concordant estimates based on ARM intensity and on  $k_{ARM}/IRM$  and  $MDF$  values provide further evidence for, first, the similarity of the coarse ferrimagnetic grain population in the two soils and, second, the presence of an additional, magnetically dominant ultra-fine grain population in the high-precipitation soil. Further, these analyses show that QDM imaging is able to separately characterize the rock magnetic properties from two distinct, intimately mixed grain populations that, together, account for approximately 100% of ferromagnetic material.

#### *Grain size estimation from precision of ARM acquisition*

The QDM's ability to measure an ARM signal from small sample volumes potentially provides a novel means for quantifying characteristic ferromagnetic grain size. The fidelity with which a sample can record the direction of an imparted thermoremanent magnetization (TRM) increases with the number of individual ferromagnetic grains present (Berndt et al., 2016). For centimeter-scale core samples containing  $\gg 10^7$  ferromagnetic grains, this statistical uncertainty is a fraction of a degree and cannot be easily quantified using typical rock magnetic measurements.

However, if isolated soil sub-volumes imaged using the QDM contain sufficiently few ferromagnetic grains on the order of  $10^5$  to  $10^6$ , this statistical scatter may range between  $1^\circ$  to  $>10^\circ$ . In comparison, optical images taken with every QDM experiment permits sample placement repeatability of  $\sim 1^\circ$ . Reproducibility of the sample mounting

orientation with respect to the ARM bias field coil is also  $<1^\circ$ . We therefore attempted to quantify the amplitude of random variations in the acquired ARM direction to estimate the number of ferromagnetic grains contained. Due to greater uncertainties associated with net moment inversions of the magnetization magnitude (Fu et al., 2020), we limited our analysis to the recovered ARM directions. Further, we focused on the distribution in ARM declination by applying an average field value subtraction, which decreases the spread of the fitted direction in inclination (Fig. 3C). Dipole inversions of declination are typically more accurate than that of inclination while, assuming isotropic sources, the variance in declination alone should provide full information on ARM reproducibility (Maxwell and Garrick-Bethell, 2020).

Importantly, applying the TRM analysis from Berndt et al. (2016) to ARM data requires an ARM acquisition process that maximizes thermally activated grain behavior. We find that ramping down the AC field at slow rates of  $1 \text{ mT s}^{-1}$  provides sufficient opportunities for thermally activated grain remagnetization that nearly all grain smaller than 140 nm would nearly reach thermal equilibrium (Supplemental Materials). Due to heat dissipation limitations on the AF coil, we were limited to a peak AF level of 50 mT for such slow ramp downs, which is sufficiently strong given the low coercivities (11.7 mT; see above) of the ultrafine magnetic sources. In total, we imparted six repeated, identical ARMs with 50 mT AC and 0.3 mT DC magnetic fields to the 420  $\mu\text{m}$ -diameter ultrafine grain sub-volume and obtained QDM magnetic field maps and net moment inversions after each ARM application.

Compilation of these fitted directions shows that the ultrafine-grained sub-volume is capable of reproducing the applied ARM direction with an angular standard deviation of  $6.2^\circ$  (Fig. 3). This level of scatter corresponds to between  $6.1 \times 10^6$  and  $9.2 \times 10^7$  discrete particles, depending on whether an empirical ARM to TRM efficiency factor of  $\sim 3.9$  is included in determining the effective bias field (Yu, 2010). Given a measured IRM of  $4.9 \times 10^{-10} \text{ Am}^2$  and a characteristic  $M_{rs}/M_s$  value for pedogenically enhanced soil of 0.15, this range of particle counts corresponds to average particle diameters of between 48 and 140 nm, assuming spherical magnetite grains. Repeating this experiment on a second,  $220 \times 250 \mu\text{m}$  sub-volume of ultrafine-grained material yields comparable estimates of 51 to 150 nm diameter grains.

These values are likely to overestimate the true typical single grain sizes because the occurrence of ferrimagnetic particles in clusters, as suggested by our electron microscopy results (see below), would partially attenuate the applied bias field through magnetostatic interactions with the backfields of neighboring particles. The degree of ARM alignment to the bias field direction would therefore be less precise in the case of clustered particles, implying that a greater number of particles would be required to achieve a given level of precision. This greater number of particles would then correspond to smaller magnetic moments and diameters for each particle. In any case, the inferred particle diameters from this analysis are significantly smaller than those

expected for windblown loess grains and directly imaged detrital grain sizes belonging to the coarse ferrimagnet population [see below; (Újvári et al., 2016)], implying a non-detrital origin for the ultrafine grain population.

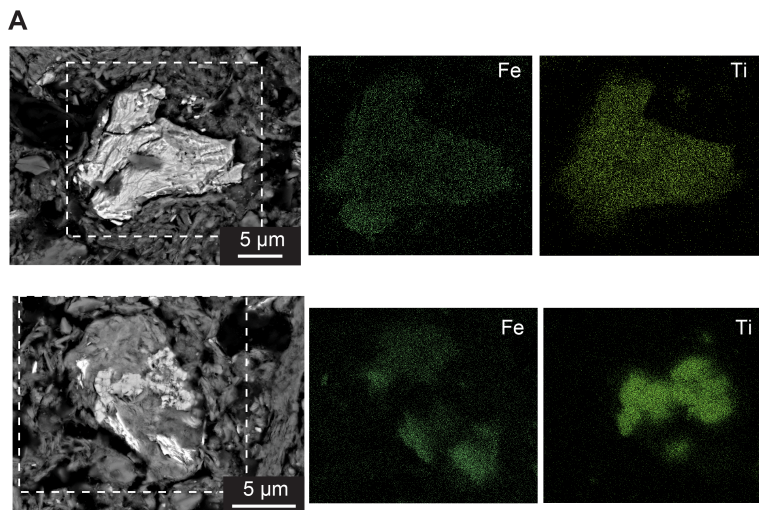


**Figure 6.** Scanning electron microscopy of coarse ferrimagnetic sources in the high-precipitation sample. The grains correspond to the labeled magnetic field sources in Fig. 2A. Left column is the BSE overview image while right columns show the distribution of Fe and Ti as detected using EDS x-ray spectroscopy.

#### *Electron microscopy*

Our rock magnetic and magnetic imaging analyses described above demonstrate the presence of two classes of ferrimagnetic grains in Qilianshan soils: a population of 0.4 - 10  $\mu\text{m}$ , coarse Fe-oxides occurring with similar concentrations in both high- and low-precipitation samples; and a population of  $\leq 150$  nm diameter grains that occur only in the high-precipitation soil. We pursued high-resolution SEM imaging and EDS analyses to image these two different ferrimagnetic grain populations and quantify their chemical composition.

For the coarse grain population, we can use QDM mapping to locate individual remanence-carrying grains for SEM and EDS analyses (Fig. 6). BSE imaging of these sources in the high-precipitation sample reveals that the host grains are typically 1-30  $\mu\text{m}$  Fe,Ti-oxides with variable Fe to Ti ratio. The size and angular morphology of these grains support an aeolian origin, which is consistent with rock magnetic characterization discussed above (Vandenberghé et al., 1997; Újvári et al., 2016).

For the ultrafine grain population, neither QDM nor optical imaging have sufficiently high resolution to isolate individual grains. We therefore first used QDM maps of a vertically-oriented, 300 mT IRM to locate the highest concentration of ferromagnetic

grains within 420  $\mu\text{m}$ -diameter ultrafine grain sub-volume. We then defined a 170 $\times$ 140  $\mu\text{m}$  region encompassing the strongest magnetic fields (Fig. 7).

Systematic survey of this region in BSE imaging mode at high magnification revealed the presence of clusters of 10s to 100s nm diameter, high atomic number ( $z$ ) grains, hereafter referred to as “ultrafine high- $z$ ” particles (Fig. 7B,C). Individual ultrafine high- $z$  grains are too small for quantitative analysis using the electron microprobe due to the longer length scale of the electron beam’s interaction volume, which results in severe mixing of characteristic x-rays from the surrounding silicates. However, given our operation at low,  $\leq 5$  keV acceleration voltages, the 1-3  $\mu\text{m}$  diameter of some clusters is significantly larger than the  $\sim 400$  nm expected interaction depth of the electron beam as estimated from Monte Carlo simulations using the CASINO v2.5.1 software (Drouin et al., 2007).

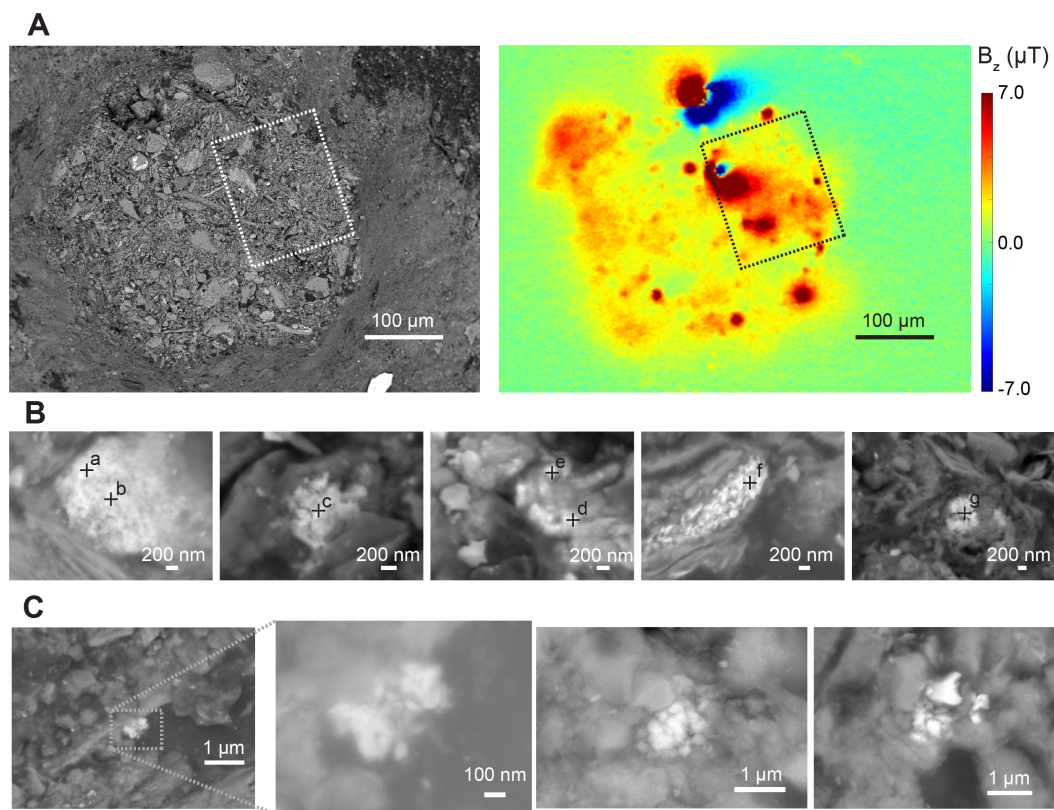


**Figure 7.** Scanning electron microscopy of ultrafine ferrimagnetic sources in the high-precipitation sample. (A) BSE map and QDM magnetic field map of the same field of view covering the  $\sim 420$   $\mu\text{m}$ -diameter ultrafine grain sub-volume. Dashed rectangle denotes the sub-region in which we looked for high- $z$  particles at high resolution using the SEM. The sample was given a 0.3 T IRM in the out-of-plane direction prior to QDM mapping. Red and blue colors correspond to out-of-plane and into-plane magnetic fields, respectively. (B) High magnification images of ferrimagnetic sources. Locations labeled a through g correspond to the sites of EDS elemental composition analysis (Table 1). (C) Additional high- $z$  particles detected in the searched region.

We therefore acquired EDS spectra of five ultrafine high-z clusters in conjunction with immediately adjacent silicates using a 5 keV acceleration voltage (Table 1). Even with the low beam interaction volume, all analyses included a minor contribution from silicates with Si content between 1.8 and 7.6 wt% with most values below 2.8%. We interpreted this component as due to mixing of characteristic x-rays from surrounding silicates and subtracted off the composition of the adjacent silicates weighted such that resulting background-subtract composition has zero Si. With this correction, the concentrations of two other silicate-forming elements, Al and Mg, both converged closer to zero for all analyses, providing support for the validity of the silicate background subtraction step. The total recovered wt% for the pre-subtracted and silicate background analyses suggest an analytical precision of ~5 wt%

We then computed the Fe:O ratio for all high-z grain clusters, finding a wide range between 0.72 and 1.19 with most values below 0.81 (Table 1). Comparing these ratios to those expected for magnetite (Fe:O = 0.75) and hematite and maghemite (Fe:O = 0.67), we find that two out of seven analyses were within uncertainty of either Fe-oxide composition. Meanwhile, three out of the seven were compatible with only magnetite while the remaining two analyses showed higher Fe:O ratios suggesting the presence of unsubtracted Fe<sup>2+</sup>, likely in silicate phases. All analyses contained Fe:O ratios closer to magnetite than hematite or maghemite. In contrast to coarse ferrimagnetic grains associated resolved magnetic sources (Fig. 6), no analyzed ultrafine high-z grain clusters contained any resolvable Ti enrichment.

## Discussion

Our joint QDM magnetic field imaging and electron microscopy analyses hold implications for understanding the mechanism of magnetic enhancement in a modern, loess-derived soil and, more generally, for establishing a new methodology for determining the mechanism of magnetic enhancement.

Multiple mechanisms have been proposed to explain well-established correlations between precipitation and soil magnetic properties. Specifically, past studies have documented, among other changes, enhanced total ferrimagnetic content, higher ARM susceptibility, and reduced mean coercivity in well-buffered soils from high-precipitation localities [e.g., Maher et al. (1994); Geiss et al. (2008); Balsam et al. (2011); Sharifigarmdareh et al. (2020); see Maxbauer et al. (2016) for review].

Bulk rock magnetic characterization of our Qilianshan soils confirm these general relationships with the higher-precipitation, low-temperature sample displaying enhanced saturation remanent magnetization, higher  $k_{ARM}/IRM$ , and lower  $MDF$  compared to the low-precipitation, high-temperature specimen (Fig. 5; Table 1). Although these bulk sample observations suggest an influence of precipitation on magnetic properties, they cannot uniquely identify the mechanism(s) producing the contrasting magnetic behaviors. As reviewed in the Introduction, these proposed

magnetic enhancement mechanisms have included compaction, changes in the detrital input, and *in situ* formation of ferrimagnets resulting from alteration of existing Fe-bearing phases or precipitation in soil pore spaces during wet and dry cycling.

QDM magnetic field imaging can aid in identifying the dominant magnetic enhancement mechanism in Qilianshan soils. QDM maps show that both high- and low-precipitation soils contain an indistinguishable population of QDM-resolvable, coarse ferrimagnetic grains with  $\sim 1 - 30 \mu\text{m}$  diameter based on both magnetic moment inversions and electron microscopy (Figs. 2, 6). The grain size distribution and Ti-composition of these grains strongly suggest a detrital origin. These observations show that any differences in deposition rate or in the composition of the aeolian input or *in situ* magnetic enhancement of coarse, detrital Fe-oxide particles do not contribute significantly to the contrasting magnetic properties of the high- and low-precipitation soils.

In contrast, QDM mapping reveals that the high-precipitation soil can acquire a strong, uniform ARM throughout the sample volume, providing evidence for an additional population of ultrafine ferromagnetic particles (Figs. 1, 3). This grain population accounts for  $88 \pm 8\%$  of the total high-precipitation sample ARM, suggesting that the formation of these ultrafine particles alone explains the  $\sim 11\times$  enhancement in  $k_{ARM}$  between the low- and high-precipitation bulk samples. Further, the fact that the proportion of ultrafine grain-carried magnetization as computed from magnetization intensity ( $\sim 88\%$ ) and from a mixing model based on  $k_{ARM}/IRM$  and  $MDF$  parameters ( $\sim 94\%$ ) are consistent within uncertainty implies that this same grain population is responsible for all observed magnetic enhancement, including the increased total magnetization, ARM susceptibility, and coercivity changes.

The relatively high  $k_{ARM}/IRM$  and very soft  $MDF$  parameters for this ultrafine population is consistent with a pedogenic origin based on comparison with previously studied modern and ancient soils, although with lower than typical  $k_{ARM}/IRM$ . Further, ARM reproducibility-based estimates of individual ultrafine grain volumes yielded individual grain diameters between  $\sim 50$  and  $140 \text{ nm}$ , which are significantly smaller than even very fine aeolian particles (Újvári et al., 2016). Together, these magnetic observations provide strong evidence that magnetic changes in the high-precipitation soil resulted from the *in situ* formation of this ultrafine ferrimagnetic particle population.

QDM data can further be used to identify the formation pathway of this ultrafine grain population. Magnetic field maps of ARM demonstrates that ultrafine grains occur uniformly throughout the high-precipitation soil with no locational relationship to coarser Fe-oxide or silicate grains (Figs. 1, 3). These authigenic ferrimagnets are therefore very unlikely to have altered directly from Fe within these reservoirs.

At the same time, the magnetic field maps allow us to identify regions that lack coarse ferrimagnetic grains while carrying strong ultrafine grain-hosted magnetization. Our SEM survey of one such region revealed  $\sim 10\text{-}300 \text{ nm}$  diameter, high-atomic number

grains that occur in micrometer-scale clusters (Fig. 7). These grains, which have diameters that overlap strongly with the size range inferred from the ARM reproducibility analysis described above, contain undetectable Ti concentrations, further demonstrating an origin independent of Ti-rich ferromagnetic grains associated with coarse magnetic field sources (Fig. 6). Previous studies have similarly demonstrated an absence of substitution by Ti or Al in pedogenic ferrites (Maher and Thompson, 1992; Ahmed and Maher, 2018).

Having identified the physical sites of magnetic enhancement, we can use EDS-derived elemental compositions to constrain the chemical pathway leading to pedogenic Fe-oxide grain formation. As discussed in the Introduction, two distinct reaction series can result in the precipitation of magnetite or maghemite from soil pore fluids, thereby accounting for the uniform occurrence of Fe-oxide grain clusters throughout the soil volume. These two mechanisms make distinct predictions for the oxidation state of pedogenic ferrimagnets. Specifically, the wet and dry cycling hypothesis predicts direct formation of  $\text{Fe}_3\text{O}_4$  (magnetite), some of which may be subsequently oxidized to  $\gamma\text{-Fe}_2\text{O}_3$  (maghemite) (Maher and Thompson, 1992; Maher, 1998; Orgeira et al., 2011; Ahmed and Maher, 2018). On the other hand, the ferrihydrite  $\rightarrow$  maghemite  $\rightarrow$  hematite transformation mechanism requires that Fe occurs in the  $\text{Fe}^{3+}$  form only during the magnetic enhancement process (Torrent et al., 2007).

Our measured Fe:O ratios for the ultrafine Fe-oxide clusters show that all imaged Fe-oxides are more consistent with the magnetite ratio of 3:4, although two out of seven clusters are within uncertainty of the 2:3 maghemite ratio (Table 1). Therefore, although we cannot rule out some contribution to the total magnetization from maghemite sources, the bulk of the ultrafine Fe-oxide population has a mixed  $\text{Fe}^{2+}$  and  $\text{Fe}^{3+}$  composition, supporting an origin during wet and dry cycling, with mobilization of  $\text{Fe}^{2+}$  in temporarily reducing conditions and its partial oxidation and precipitation upon subsequent drying and re-oxidation of soil micro-environments (Maher and Thompson, 1992).

An additional distinguishing characteristic between these two mechanisms of pedogenic ferrimagnet formation is the presence of Al substitution in the Fe-oxide phases, which is expected for the ferrihydrite  $\rightarrow$  maghemite  $\rightarrow$  hematite pathway. Specifically, visible diffuse reflectance spectrum measurements have been used on CLP paleosols to show that pedogenic hematite has lower  $P_{560}$  values between ~530 and 545 nm (Hu et al., 2013). This parameter, which quantifies the shift in an electron transition energy as inferred from changes in the reflectance spectrum, has been measured for a range of synthetic, Al-substituted hematites (Kosmas, 1986; Liu et al., 2011). These calibration studies have measured  $P_{560}$  values below 545 nm only in samples with at least 4 molar percent (mol%; equivalent to 3.3 wt% for an  $\text{Fe}_2\text{O}_3$  composition) Al substitution, with most samples in the  $P_{560} = 530\text{-}545$  containing 5-13 mol% (4.1-10.8 wt%) Al. No Fe-oxide clusters from our EDS analyses contain greater than 3.5 mol%, while the two Fe-oxide clusters from our analyses that have Fe:O ratio compatible with  $\text{Fe}_2\text{O}_3$  have a

maximum Al content of only 2.7 wt% (Table 1). The uncertainties on these measured Al contents are likely on the order of several percent, preventing us from conclusively excluding larger Al enrichments. Nevertheless, these low Al contents are most compatible with a magnetite-forming pathway, which specifically precludes Al substitution (Taylor et al., 1986).

In terms of rock magnetism techniques, our study demonstrates several novel uses of high-resolution magnetic field imaging. First, we have shown that QDM magnetic field imaging is capable of accurately quantifying remanence-based rock magnetic parameters such as remanent magnetization intensity, remanence susceptibility, and remanence coercivity directly from individual magnetic grain populations, even if distinct grains types are intimately mixed. In the case of our high-precipitation soil, QDM measurements provided the  $k_{ARM}/IRM$  and AF demagnetization spectra of ultrafine ferrimagnetic grains after numerical subtraction of confounding coarse grained sources. The location of this ultrafine grain population in  $k_{ARM}/IRM - MDF$  space on a mixing curve determined from bulk sample measurements confirms the accuracy of these recovered parameters (Fig. 5).

Second, our analysis of the coarse ferrimagnetic grain population shows that quantitative net moment inversion, applied over several hundred sources, can generate a statistically meaningful representation of individual grain moment and estimated diameter distributions. This information can be used to characterize directly magnetic differences in aeolian precursor grains and to document any magnetic enhancement within this population. The QDM can therefore serve as a rapid method for assessing changes in rock magnetic properties arising from provenance variations or coarse Fe-oxide alteration rather than from authigenic ferrimagnets. Establishing the relative magnitudes of detrital and pedogenic contributions is key to determining whether climofunctions based on the growth of ultrafine ferrimagnets can be reliably applied. This capability may be especially important to study areas with less well-established evidence for a high degree of aeolian grain mixing and uniformity compared to the CLP (Maher et al., 2009).

Third, QDM magnetic field maps can reveal potential spatial associations between magnetic sources and, for example, other Fe-bearing phases from which they are altered. In the case of Qilianshan soils, the lack of correlation between ultrafine grains and detrital Fe-bearing phases and the disseminated distribution of ultrafine grains provide evidence for pore space ferrimagnet precipitation. Imaging of magnetic particles locations also enables follow-up analysis using, for example, electron microscopy to quantify grain size and composition.

Finally, we have isolated sufficiently small volumes of ferromagnetic carriers such that the statistical uncertainty in reproducing a laboratory ARM can be used as a direct estimator of grain number density and, therefore, grain size. Future work potentially

involving micromagnetic modeling of interactions can potentially further exploit this data type to characterize the size and spatial distribution of unresolved grains.

## Conclusions

Our investigation into a pair of high- and low-rainfall soils from the Qilianshan Range was designed to evaluate the contribution of different proposed mechanisms to bulk soil magnetic enhancement and resultant rock magnetic changes. We developed and applied several high-resolution magnetic field imaging techniques to isolate the signal from distinct ferrimagnetic grain populations within the soil samples. This analysis led to the identification of two distinct ferrimagnetic particle populations. First, a coarse, 1-30  $\mu\text{m}$  diameter population of Fe-oxide and Fe,Ti-oxide grains are present in both soil types, carrying  $\sim 10\%$  and  $\sim 100\%$  of the total ARM in the high- and low-precipitation samples, respectively. The grain size and angular morphology of these coarse grains suggest an aeolian origin, while the lack of differences in the concentration and single-grain magnetization distributions between the two different soils indicate the lack of any climate-related magnetic changes within these grains.

Second, an ultrafine population of ferrimagnetic particles is present only at the high-precipitation locality and constitutes  $\sim 90\%$  of the total sample ARM. This population occurs throughout the entire sample volume, unrelated to the location of detrital magnetic grains, and exhibits high  $k_{ARM}/IRM$  ratio and soft coercivity compared to the aeolian ferrimagnetic grains. These traits are hallmarks of magnetically enhanced soils. EDS compositional measurements indicate a magnetite composition, strongly suggest that these grains formed during wet and dry cycling causing  $\text{Fe}^{2+}$  mobilization and subsequent precipitation of magnetite.

The pervasive presence of ultrafine magnetite grains in the higher precipitation soil is consistent with similar findings based on bulk sample rock magnetic analysis and electron microscopy studies (Maher and Thompson, 1991, 1992; Evans and Heller, 1994; Ahmed and Maher, 2018). Magnetic field imaging augments this picture in several ways. First, quantifying the magnetization of individual coarse ferrimagnetic grains permits the direct inference that the aeolian grain population has indistinguishable rock magnetic properties in the two localities and, therefore, that these grains did not participate in moisture-driven magnetic enhancement. Second, the sub-uniform distribution of the ultrafine grains confirms that, at least in these studied samples, pedogenic enhancement occurred throughout the sample volume and was not associated with precursor Fe-bearing silicates or oxides. Finally, magnetic imaging provides a framework for linking further non-magnetic characterization, such as electron microscopy, to specific magnetic grain populations.

Together, these insights provide strong constraints on the mechanism of magnetic enhancement in Qilianshan soils, demonstrating a set of methods that can potentially be

widely applied to paleosol and loess samples to determine the pathway of magnetic enhancement and verify the applicability of quantitative paleorainfall reconstructions.

### **Acknowledgements**

We thank M.W.R. Volk for discussions that improved the manuscript. RRF was funded by grants from the National Science Foundation (AGS-2202772) and the Lemann Brazil Fund.

### **Open Research**

Data Availability Statement: Data types for this work consist of QDM magnetic field maps, text files of net magnetization fitting results, bulk soil sample data from the 2G superconducting rock magnetometer, and SEM microscopy images and compositional maps. All data is publicly available on the Harvard Dataverse archive (Fu et al., 2022).

**Table 1: Background-subtracted EDS compositions of ultrafine high-z clusters**

Point ID	O	Na	Mg	Al	S	Ca	Ti	Fe	Si (Pre-subtraction)	High-z Point Total	Bkg. Point Total	Fe:O Atomic Ratio
a	26.9	0.1	0.5	0.6	0.21	0.7	0.0	70.5	1.8	106.8	95.9	0.75
b	23.9	0.1	0.5	0.6	0.18	0.8	0.0	59.9	2.4	95.6	95.9	0.72
c	25.1	0.2	0.6	3.5	0.0	0.0	0.0	71.3	2.2	105.7	87.2	0.81
d	21.5	0.0	0.9	2.2	0.0	1.3	0.0	58.6	4.6	106.7	87.1	0.78
e	14.9	0.1	0.1	2.7	0.2	4.0	0.0	37.3	7.6	94.9	87.1	0.72
f	22.3	0.1	0.0	0.0	0.0	0.0	0.0	71.2	1.6	104.9	94.8	0.92
g	14.9	0.0	0.2	0.0	0.0	0.7	0.0	61.2	3.7	99.4	96.4	1.18

Notes: All values except for Fe:O ratio are given in weight percent (wt%). Elemental columns give the composition of each high-z point after subtraction of silicate background assuming the high-z clusters do not contain Si. The “Si (Pre-subtraction)” column gives the wt% of Si in the original high-z cluster measurement. The two “Total” columns provide the total wt% of the high-z and surrounding silicate analyses. These three columns are designed to constrain the precision of the background-subtracted composition. The “Fe:O Atomic Ratio” column is computed from the background-subtracted elemental concentrations. For comparison, the Fe:O atomic ratios of stoichiometric magnetite, hematite, and maghemite are 0.75, 0.67, and 0.67, respectively.

## References

- Ahmed, I.A.M., and Maher, B.A., 2018, Identification and paleoclimatic significance of magnetite nanoparticles in soils: *Proceedings of the National Academy of Sciences*, v. 115, p. 1736–1741, doi:10.1073/pnas.1719186115.
- Balsam, W.L., Ellwood, B.B., Ji, J., Williams, E.R., Long, X., and El Hassani, A., 2011, Magnetic susceptibility as a proxy for rainfall: Worldwide data from tropical and temperate climate: *Quaternary Science Reviews*, v. 30, p. 2732–2744, doi:10.1016/j.quascirev.2011.06.002.
- Berndt, T., Muxworthy, A.R., and Fabian, K., 2016, Does size matter? Statistical limits of paleomagnetic field reconstruction from small rock specimens: *J. Geophys. Res. Solid Earth*, v. 121, p. 15–26, doi:10.1002/2015JB012441.
- Chen, T., Xu, H., Xie, Q., Chen, J., Ji, J., and Lu, H., 2005, Characteristics and genesis of maghemite in Chinese loess and paleosols: Mechanism for magnetic susceptibility enhancement in paleosols: *Earth Planet. Sci. Lett.*, v. 240, p. 790–802, doi:10.1016/j.epsl.2005.09.026.
- Drouin, D., Couture, A., Joly, D., Tastet, X., Aimez, V., and Gauvin, R., 2007, CASINO V2.42—A Fast and Easy-to-use Modeling Tool for Scanning Electron Microscopy and Microanalysis Users: *Scanning*, v. 29.
- Egli, R., 2004, Characterization of individual rock magnetic components by analysis of remanence curves: 1. Unmixing natural sediments: *Stud. Geophys. Geod.*, v. 48, p. 391–446.
- Evans, M.E., and Heller, F., 1994, Magnetic Enhancement and Palaeoclimate: Study of A Loess/Palaeosol Couplet Across the Loess Plateau of China: *Geophys. J. Int.*, v. 117, p. 257–264, doi:10.1111/j.1365-246X.1994.tb03316.x.
- Fu, R.R., Lima, E.A., Volk, M.W.R., and Trubko, R., 2020, High sensitivity moment magnetometry with the quantum diamond microscope: *Geochem. Geophys. Geosyst.*, v. 21, p. e2020GC009147.
- Fu, R.R., Maher, B.A., Nie, J., Gao, P., Berndt, T., and Cavanaugh, T., 2022, Replication Data for: Pinpointing the mechanism of magnetic enhancement in modern soils using high-resolution magnetic field imaging: <https://doi.org/10.7910/DVN/Z4CBN8>.
- Gao, P., Nie, J., Yan, Q., Zhang, X., Liu, Q., Cao, B., and Pan, B., 2021, Millennial Resolution Late Miocene Northern China Precipitation Record Spanning Astronomical Analogue Interval to the Future: *Geophysical Research Letters*, v. 48, doi:10.1029/2021GL093942.
- Geiss, C.E., Egli, R., and Zanner, W., 2008, Direct estimates of pedogenic magnetite as a tool to reconstruct past climates from buried soils: *J. Geophys. Res.*, v. 113, p. B11102.

- Glenn, D.R., Fu, R.R., Kehayias, P., Le Sage, D., Lima, E.A., Weiss, B.P., and Walsworth, R.L., 2017, Micrometer-scale magnetic imaging of geological samples using a quantum diamond microscope: *Geochemistry, Geophysics, Geosystems*, v. 18, p. 2017GC006946, doi:10.1002/2017GC006946.
- Groot, L.V., Fabian, K., Béguin, A., Kusters, M.E., Cortés-Ortuño, D., Fu, R.R., Jansen, C.M.L., Harrison, R.J., Leeuwen, T., and Barnhoorn, A., 2021, Micromagnetic Tomography for Paleomagnetism and Rock-Magnetism: *Journal of Geophysical Research: Solid Earth*, v. 126, doi:10.1029/2021JB022364.
- Heller, F., and Liu, T.-S., 1984, Magnetism of Chinese loess deposits: *Geophysical Journal International*, v. 77, p. 125–141, doi:10.1111/j.1365-246X.1984.tb01928.x.
- Heller, F., and Liu, T.-S., 1986, Palaeoclimatic and sedimentary history from magnetic susceptibility of loess in China: *Geophysical Research Letters*, v. 13, p. 1169–1172, doi:10.1029/GL013i011p01169.
- Hu, P., Liu, Q., Torrent, J., Barrón, V., and Jin, C., 2013, Characterizing and quantifying iron oxides in Chinese loess/paleosols: Implications for pedogenesis: *Earth and Planetary Science Letters*, v. 369–370, p. 271–283, doi:10.1016/j.epsl.2013.03.033.
- Kosmas, C.S., 1986, Relationship among Derivative Spectroscopy, Color, Crystallite Dimensions, and Al Substitution of Synthetic Goethites and Hematites 1: *Clays and Clay Minerals*, v. 34, p. 625–634, doi:10.1346/CCMN.1986.0340602.
- Kukla, G., Heller, F., Ming, L.X., Chun, X.T., Sheng, L.T., and Sheng, A.Z., 1988, Pleistocene climates in China dated by magnetic susceptibility: *Geology*, v. 16, p. 811, doi:10.1130/0091-7613(1988)016<0811:PCICDB>2.3.CO;2.
- Lima, E.A., and Weiss, B.P., 2016, Ultra-high sensitivity moment magnetometry of geological samples using magnetic microscopy: *Geochem. Geophys. Geosyst.*, v. 17, p. 3754–3774, doi:10.1002/2016GC006487.
- Liu, Q., Barrón, V., Torrent, J., Eeckhout, S.G., and Deng, C., 2008, Magnetism of intermediate hydromaghemite in the transformation of 2-line ferrihydrite into hematite and its paleoenvironmental implications: *Journal of Geophysical Research*, v. 113, p. B01103, doi:10.1029/2007JB005207.
- Liu, Q.S., Torrent, J., Barrón, V., Duan, Z.Q., and Bloemendal, J., 2011, Quantification of hematite from the visible diffuse reflectance spectrum: effects of aluminium substitution and grain morphology: *Clay Minerals*, v. 46, p. 137–147, doi:10.1180/claymin.2011.046.1.137.
- Maher, B.A., 1998, Magnetic properties of modern soils and Quaternary loessic paleosols: paleoclimatic implications: *Palaeogeography, Palaeoclimatology, Palaeoecology*, v. 137, p. 25–54, doi:10.1016/S0031-0182(97)00103-X.

- Maher, B.A., 1988, Magnetic properties of some synthetic sub-micron magnetites: *Geophys. J.*, v. 94, p. 83–96.
- Maher, B.A., 2016, Palaeoclimatic records of the loess/palaeosol sequences of the Chinese Loess Plateau: *Quaternary Science Reviews*, v. 154, p. 23–84, doi:10.1016/j.quascirev.2016.08.004.
- Maher, B.A., Alekseev, A., and Alekseeva, T., 2003, Magnetic mineralogy of soils across the Russian Steppe: climatic dependence of pedogenic magnetite formation: *Palaeogeography, Palaeoclimatology, Palaeoecology*, v. 201, p. 321–341, doi:10.1016/S0031-0182(03)00618-7.
- Maher, B.A., Mutch, T.J., and Cunningham, D., 2009, Magnetic and geochemical characteristics of Gobi Desert surface sediments: Implications for provenance of the Chinese Loess Plateau: *Geology*, v. 37, p. 279–282.
- Maher, B.A., and Possolo, A., 2013, Statistical models for use of palaeosol magnetic properties as proxies of palaeorainfall: *Global and Planetary Change*, v. 111, p. 280–287.
- Maher Taylor, R., 1988, . Formation of ultrafine-grained magnetite in soils. *Nature*, Vol. 336, p. 368-370.:
- Maher, B.A., and Thompson, R., 1991, Mineral magnetic record of the Chinese loess and paleosols: *Geology*, v. 19, p. 3, doi:10.1130/0091-7613(1991)019<0003:MMROTC>2.3.CO;2.
- Maher, B.A., and Thompson, R., 1992, Paleoclimatic Significance of the Mineral Magnetic Record of the Chinese Loess and Paleosols: *Quaternary Res.*, v. 37, p. 155–170, doi:10.1016/0033-5894(92)90079-X.
- Maher, B.A., Thompson, R., and Zhou, L.P., 1994, Spatial and temporal reconstructions of changes in the Asian palaeomonsoon: A new mineral magnetic approach: *Earth Planet. Sci. Lett.*, v. 125, p. 461–471.
- Maxbauer, D.P., Feinberg, J.M., and Fox, D.L., 2016, Magnetic mineral assemblages in soils and paleosols as the basis for paleoprecipitation proxies: A review of magnetic methods and challenges: *Earth-Science Reviews*, v. 155, p. 28–48, doi:10.1016/j.earscirev.2016.01.014.
- Maxwell, R.E., and Garrick-Bethell, I., 2020, Evidence for an Ancient Near-Equatorial Lunar Dipole From Higher Precision Inversions of Crustal Magnetization: *Journal of Geophysical Research: Planets*, v. 125, doi:10.1029/2020JE006567.
- McGee, D., 2020, Glacial–Interglacial Precipitation Changes: *Annual Review of Marine Science*, v. 12, p. 525–557, doi:10.1146/annurev-marine-010419-010859.

- Nie, J., King, J.W., and Fang, X., 2008, Link between benthic oxygen isotopes and magnetic susceptibility in the red-clay sequence on the Chinese Loess Plateau: *Geophysical Research Letters*, v. 35, p. L03703, doi:10.1029/2007GL032817.
- Nie, J., Song, Y., King, J.W., and Egli, R., 2010, Consistent grain size distribution of pedogenic maghemite of surface soils and Miocene loessic soils on the Chinese Loess Plateau: *ROCK MAGNETISM, SURFACE SOILS AND MIOCENE LOESSIC SOILS: Journal of Quaternary Science*, v. 25, p. 261–266, doi:10.1002/jqs.1304.
- Orgeira, M.J., Egli, R., and Compagnucci, R., 2011, A quantitative model of magnetic enhancement in loessic soils, *in The Earth's Magnetic Interior*, Dordrecht, Springer, p. 361–397.
- Roberts, A.P., Almeida, T.P., Church, N.S., Harrison, R.J., Heslop, D., Li, Y., Li, J., Muxworthy, A.R., Williams, W., and Zhao, X., 2017, Resolving the Origin of Pseudo-Single Domain Magnetic Behavior: *Journal of Geophysical Research: Solid Earth*, v. 122, p. 9534–9558, doi:10.1002/2017JB014860.
- Sharifigarmdareh, J., Khormali, F., Scheidt, S., Rolf, C., Kehl, M., and Frechen, M., 2020, Investigating soil magnetic properties with pedogenic variation along a precipitation gradient in loess-derived soils of the Golestan province, northern Iran: *Quaternary International*, v. 552, p. 100–110, doi:10.1016/j.quaint.2019.11.022.
- Shepherd, T.G., 2014, Atmospheric circulation as a source of uncertainty in climate change projections: *Nature Geosci.*, v. 7, p. 703–708.
- Sun, Y., Clemens, S.C., An, Z., and Yu, Z., 2006, Astronomical timescale and palaeoclimatic implication of stacked 3.6-Myr monsoon records from the Chinese Loess Plateau: *Quaternary Science Reviews*, v. 25, p. 33–48, doi:10.1016/j.quascirev.2005.07.005.
- Taylor, R.M., Maher, B.A., and Self, P.G., 1986, Magnetite in soils: I. The synthesis of single-domain and superparamagnetic magnetite: *Clay Minerals*, v. 22, p. 411–422, doi:10.1180/claymin.1987.022.4.05.
- Torrent, J., Barrón, V., and Liu, Q., 2006, Magnetic enhancement is linked to and precedes hematite formation in aerobic soil: *Geophysical Research Letters*, v. 33, p. L02401, doi:10.1029/2005GL024818.
- Torrent, J., Liu, Q., Bloemendal, J., and Barrón, V., 2007, Magnetic Enhancement and Iron Oxides in the Upper Luochuan Loess-Paleosol Sequence, Chinese Loess Plateau: *Soil Science Society of America Journal*, v. 71, p. 1570–1578, doi:10.2136/sssaj2006.0328.
- Újvári, G., Kok, J.F., Varga, G., and Kovács, J., 2016, The physics of wind-blown loess: Implications for grain size proxy interpretations in Quaternary paleoclimate studies: *Earth-Science Reviews*, v. 154, p. 247–278, doi:10.1016/j.earscirev.2016.01.006.
- Vandenbergh, J., Zhisheng, A., Nugteren, G., Huayu, L., and Van Huissteden, K., 1997, New absolute time scale for the Quaternary climate in the Chinese Loess region by grain-size

analysis: *Geology*, v. 25, p. 35, doi:10.1130/0091-7613(1997)025<0035:NATSFT>2.3.CO;2.

- Volk, M.W.R., Fu, R.R., Trubko, R., Kehayias, P., Glenn, D.R., and Lima, E.A., 2022, QDMLab: A MATLAB toolbox for analyzing quantum diamond microscope (QDM) magnetic field maps.: *Comput. Geosci.*, v. 167, p. 105198.
- Xiao, G., Zong, K., Li, G., Hu, Z., Dupont-Nivet, G., Peng, S., and Zhang, K., 2012, Spatial and glacial-interglacial variations in provenance of the Chinese Loess Plateau: *Geophys. Res. Lett.*, v. 39, p. L20715.
- Yang, T., Hyodo, M., Zhang, S., Maeda, M., Yang, Z., Wu, H., and Li, H., 2013, New insights into magnetic enhancement mechanism in Chinese paleosols: *Palaeogeog. Palaeoclimatol. Palaeoecol.*, v. 369, p. 493–500, doi:10.1016/j.palaeo.2012.11.016.
- Yu, Y., 2010, Paleointensity determination using anhysteretic remanence and saturation isothermal remanence: *Geochem. Geophys. Geosyst.*, v. 11, p. Q02Z12, doi:10.1029/2009GC002804.
- Zhang, H., Nie, J., Liu, X., Pullen, A., Li, G., Peng, W., and Zhang, H., 2021, Spatially variable provenance of the Chinese Loess Plateau: *Geology*, v. 49.

# Pinpointing the mechanism of magnetic enhancement in modern soils using high-resolution magnetic field imaging

Roger R. Fu<sup>1</sup>, Barbara A. Maher<sup>2</sup>, Junsheng Nie<sup>3</sup>, Peng Gao<sup>3</sup>, Thomas Berndt<sup>4</sup>, Elizabeth Folsom<sup>1</sup>, Timothy Cavanaugh<sup>5</sup>

<sup>1</sup>Department of Earth and Planetary Sciences, Harvard University, Cambridge, Massachusetts, USA.

<sup>2</sup>Centre for Environmental Magnetism and Palaeomagnetism, Lancaster Environment Centre, University of Lancaster, Lancaster, United Kingdom

<sup>3</sup>Key Laboratory of Western China's Environment System (Ministry of Education), College of Earth and Environmental Sciences, Lanzhou University, Lanzhou, China

<sup>4</sup>Department of Geophysics, School of Earth and Space Sciences, Peking University, Beijing, China

<sup>5</sup>Center for Nanoscale Systems, Harvard University, Cambridge, Massachusetts, USA.

## Abstract

In well-buffered modern soils, higher annual rainfall is associated with enhanced soil ferrimagnetic mineral content, especially of ultrafine particles that result in distinctive observable rock magnetic properties. Hence, paleosol magnetism has been widely used as a paleoprecipitation proxy. Identifying the dominant mechanism(s) of magnetic enhancement in a given sample is critical for reliable inference of paleoprecipitation. Here we use high-resolution magnetic field and electron microscopy to identify the grain-scale setting and formation pathway of magnetic enhancement in two modern soils developed in higher (~580 mm/y) and lower (~190 mm/y) precipitation settings from the Qilianshan Range, China. We find both soils contain 1-30  $\mu\text{m}$  aeolian Fe-oxide grains with indistinguishable rock magnetic properties while the higher-precipitation soil contains an additional population of ultrafine (<150 nm), magnetically distinct magnetite grains. We show that the *in situ* precipitation of these ultrafine particles, likely during wet-dry cycling, is the only significant magnetic enhancement mechanism in this soil. These results demonstrate the potential for quantum diamond microscope (QDM) magnetic microscopy to extract magnetic information from distinct, even intimately mixed, grain populations. This information can be used to evaluate the contribution of distinct enhancement mechanisms to the total magnetization.

## Plain Language Summary

Reconstructing how natural climate variations in the past influenced rainfall patterns is important for understanding how rainfall would respond to our currently changing climate. The amount and properties of microscopic, magnetic minerals in soil can change due to interactions with pore water; therefore, characterizing the magnetic properties of soils can aid in quantifying past rainfall. We use the quantum diamond microscope

(QDM) a device that allows micrometer-scale mapping of magnetic sources in rock and soil samples, to investigate the magnetic properties of two soils formed in low- and high-rainfall environments. We find that, although both soils contain wind-blown, magnetic dust, only the high-rainfall soil contains an abundant, highly magnetic population of magnetite grains formed in soil pore spaces during repeated cycles of wetting and drying. These observations demonstrate the dominant pathway by which soil magnetism responds to rainfall and showcase the ability of QDM mapping to reliably identify the mechanism of magnetism modification in soils.

## Introduction

The challenge of understanding how patterns of rainfall will respond to a changing climate has motivated the study of ancient precipitation during times of natural climate variability (Shepherd, 2014; McGee, 2020). Paleosols developed in and interbedded with continental-scale loess deposits represent a proxy for ancient precipitation regimes. In particular, the Chinese Loess Plateau (CLP) has been the subject of focused investigation due to its unique record comprising ~350 m of sediments deposited quasi-continuously over the past >2.6 million years (My) (Maher, 2016). Robust correlations between the magnetic susceptibility of CLP deposits, Milankovitch cyclicity, and established archives such as the marine benthic  $\delta^{18}\text{O}$  record have demonstrated that paleoclimate information is encoded in the magnetism of CLP sediments (Heller and Liu, 1984; Maher and Thompson, 1992; Sun et al., 2006; Nie et al., 2008; Maher, 2016).

Understanding the paleoclimatic implications of the CLP magnetism record requires identification of the physical condition or conditions that lead to magnetic enhancement. Early studies hypothesized that preferential soil compaction during wet intervals or variations in non-magnetic dust deposition rates can explain the link between hydrological environment and magnetism (Heller and Liu, 1986; Kukla et al., 1988).

Subsequent studies have discovered and quantified distinct coarse ( $\geq 2 \mu\text{m}$  diameter) and ultrafine ( $\leq 100 \text{ nm}$ ) populations of ferrimagnetic grains in CLP paleosols (Maher and Thompson, 1991, 1992). Similarities between the paleosol ultrafine population and magnetite particles formed in laboratory reactions under soil-like conditions have led to the now widely accepted model that magnetically enriched intervals in the CLP frequently represent times of enhanced rainfall, which led to enhanced redox activity and *in situ* formation of the ultrafine ferrimagnetic grains (Maher and Taylor, 1988).

Multiple physical models have been proposed for the formation of ultrafine ferrimagnetic particles. Based on a comparison of soils from a range of climatic conditions and laboratory synthesis experiments (Maher and Taylor, 1988), Maher (1998) proposed that repeated wetting and drying cycles can lead to the precipitation of ultrafine magnetite, likely aided by  $\text{Fe}^{3+}$ -reducing bacteria, while simultaneously preventing wholesale oxidation of these ultrafine products into weakly magnetic  $\text{Fe}^{3+}$  phases such as goethite and hematite. High-resolution electron microscopy suggests that magnetite,

rather than maghemite, dominates the mineralogy of the ultrafine pedogenic ferrimagnets (Ahmed and Maher, 2018). Quantitative modeling of this process and comparison to the magnetism-rainfall relationship, or climofunction, of modern soils appear to support its occurrence across a wide range of rainfall regimes up to ~1000 mm y<sup>-1</sup> (Maher et al., 2003; Geiss et al., 2008; Orgeira et al., 2011; Balsam et al., 2011). According to this model, pedogenic magnetic content in ancient deposits such as those of the CLP is a quantitative indicator of rainfall amount (Maher and Possolo, 2013), modified in some locations by soil water changes due to evapotranspiration (Orgeira et al., 2011).

Other authors, however, have attributed enrichment of ultrafine ferrimagnets to direct oxidation of aeolian Fe-oxides or concentration of preexisting silicate-hosted Fe-oxide particles. Maghemite found in association with coarser aeolian magnetite provides evidence for ultrafine maghemite production from magnetite oxidation, although the proportional contribution of this pathway to total soil magnetic enhancement is unclear (Chen et al., 2005). Meanwhile, scanning electron microscopy (SEM) observations of CLP paleosols have revealed higher abundance of coarse (>10 µm) silicate minerals containing abundant <100 nm scale ferrimagnets in soils with strongest magnetic enhancement (Yang et al., 2013). Although ferrimagnetic grain formation via these pathways may also depend on local climate, additional factors such as the concentration of magnetite and Fe-bearing silicates in the unmodified aeolian source are also suggested to play a role.

A final proposed pathway for forming pedogenic ferrimagnets involves the transformation of ferrihydrite to single domain maghemite, rather than magnetite, and ultimately to hematite without a role for wetting and drying cycles and the accompanying reducing conditions. Correlations between the concentration of ultrafine ferrimagnets and hematite in natural soils and observed growth of similar-sized maghemite in laboratory experiments have provided support for this mechanism (Torrent et al., 2006, 2007; Liu et al., 2008). If validated, this origin for soil magnetic enhancement implies that higher ferrimagnetic content is an indicator for warmer temperatures, which favors the transformation of Fe<sup>3+</sup> in ferrihydrite into maghemite and hematite instead of into weakly magnetic goethite.

In summary, different mechanisms of magnetic enhancement may be dominant depending on the specific soil composition and environment. Because these models predict distinct relationships between magnetic enhancement and climatic conditions, the dominant mechanism of magnetic enhancement in an ancient sample must be identified before paleoclimatic inferences can be made.

As a further complication, multiple enhancement mechanisms with distinct relationships to rainfall may act simultaneously on the same sample. For example, the provenance of aeolian grains to the CLP varied significantly in both time and space (Xiao et al., 2012; Zhang et al., 2021). Hence, even if a similar process of *in situ* magnetic grain growth process occurred in multiple samples, their magnetic properties and the degree

of authigenic enhancement may depend on the composition of aeolian precursors as well as the degree of rainfall-induced enhancement.

Detailed microscopy of modern and ancient soils may aid in identifying the mechanism(s) of magnetic enhancement. Identification of ferrimagnetic grains co-occurring with, for example, detrital Fe-oxides or Fe-bearing silicates may provide evidence for their formation from these precursors. In parallel, crystallographic and compositional studies can distinguish between magnetite and maghemite along with the concentration of substitutional trace elements. For example, lattice-scale observations of soil ferrimagnets have identified Al-poor magnetite as the main contributor to magnetism in a modern soil from the UK and some CLP paleosols (Ahmed and Maher, 2018). This observation appears inconsistent with the ferrihydrite → maghemite → hematite pathway described above, which produces Fe-oxides with several atomic percent Al<sup>3+</sup> substitution (Hu et al., 2013).

In this work, we use the quantum diamond microscope (QDM), a recently developed high-resolution magnetic field imager, to aid in understanding the mechanism of magnetic enhancement in modern soils from the Qilianshan Range, China, that developed in high-rainfall/low-temperature and low-rainfall/high-temperature settings. First, we use the high spatial resolution of the QDM to distinguish populations of ferrimagnetic grains within the soils and obtain magnetic information from each sub-population. We use this grain-scale magnetic characterization to constrain the physical location and chemical pathway of magnetic enhancement. Second, we use QDM maps to localize regions with high concentrations of magnetic sources to guide electron microscopy-based analyses of ferrimagnetic grains, thereby directly linking the source of magnetism to detailed analyses of grain composition.

## **Samples and Methods**

We collected A horizon soil samples between 5 and 10 cm depth from a transect in the Qilianshan Range representing a range of elevations to study how local temperature and rainfall correlate with differences in magnetic properties (Gao et al., 2021). These soils were developed in loessic parent material on the northern flank of the Qilianshan Range, which receives predominantly summer precipitation. The highest and lowest elevation samples were collected from 3533 m (101.85° E, 37.56° N) and 1859 m (102.3° E, 37.94° N) above sea level (Fig. S11 in Gao et al., 2021). The annual mean precipitation at these two sites is, respectively, 576.6 and 192.8 mm based on linear interpolation and extrapolation of annual mean precipitation data obtained between 2011 and 2020 from four meteorological stations at elevations of 2060 m (242.6 mm), 2710 m (403.9 mm), 3070 m (523.3mm), and 3600 m (584.3 mm) above sea level of the Qilianshan Range. The annual mean and summer mean air temperatures at the high-elevation, higher-precipitation site over the same period are -2.0°C and 6.9°C while those for the low-elevation, low-precipitation site are 9.6°C and 21.4°C.

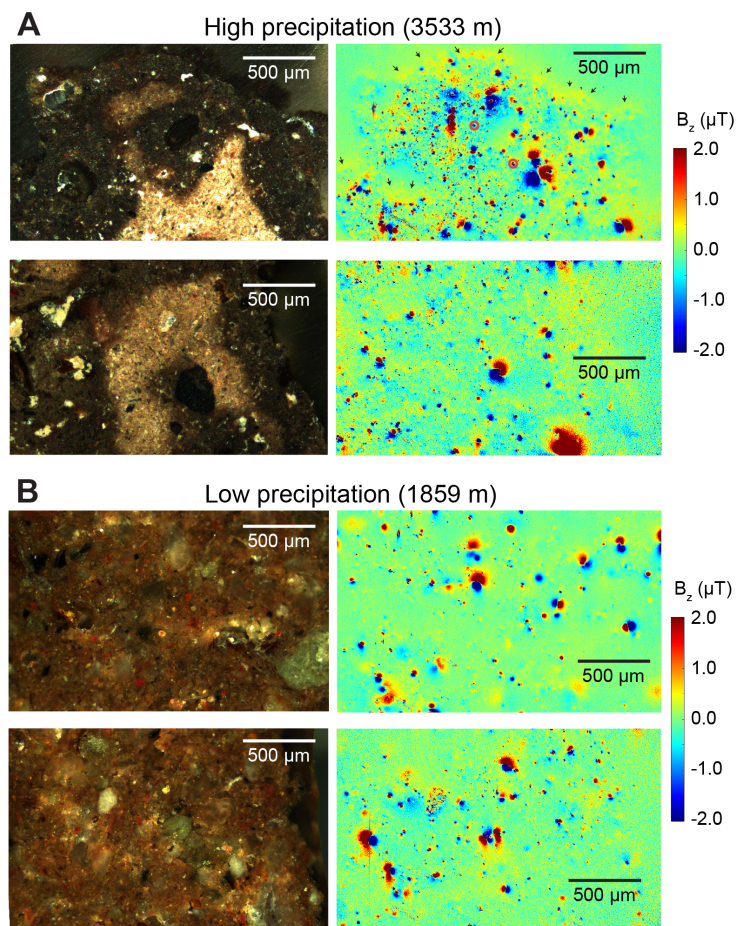


**Figure 1.** Representative QDM magnetic field maps of (A) high-elevation, high-rainfall, low-temperature and (B) low-elevation, low-rainfall, high-temperature modern soils. Photomicrographs in the left column were taken in reflected light with crossed polars. Positive (negative) values denote magnetic fields oriented out of (into) the page. All samples carry an ARM with bias field in the 12 o'clock direction. Note the diffuse positive magnetic fields at the 12 o'clock edge of the sample visible in the topmost QDM map (small black arrows). These fringing fields indicate the presence of an unresolved, fine grain population carrying a uniform magnetization. The two sources in red circles in panel (A) were further analyzed using electron microscopy in Fig. 6.

Once the dry soil samples arrived in the in the Harvard Paleomagnetism Lab, we first vacuum impregnated approximately 40 mm<sup>3</sup> volume of each using Epo-tek® 301 epoxy. The absence of detectable magnetic field signal outside the soil regions in QDM maps demonstrates the magnetic cleanness of the epoxy (Fig. 1). We then cut and polished a ~300 μm thick section for each sample. We performed QDM magnetic field imaging in

projected magnetic microscopy (PMM) mode in a 0.9 mT bias magnetic field that was reversed during data acquisition, resulting in a 700 nT uncanceled field (Glenn et al., 2017). Most QDM magnetic field maps were integrated over  $\sim 30$  minutes. The raw QDM data were then processed using GPU microwave spectra fitting routines in the *QDMLab* software package with a global fluorescence factor of 0.25 (Fu et al., 2020; Volk et al., 2022). Prior to the QDM experiments, we applied anhysteretic remanent magnetizations (ARM), isothermal remanent magnetizations (IRM), and alternating field (AF) demagnetization to the samples using the AC and DC coils on a 2G Enterprises model 755 superconducting rock magnetometer with installed RAPID system in the Harvard Paleomagnetism Lab. Bulk measurements of 5-10 mm sized blocks of the same soil samples were conducted with the same 2G Enterprises magnetometer. All data used in this study are available on the Harvard Dataverse (Fu et al., 2022).

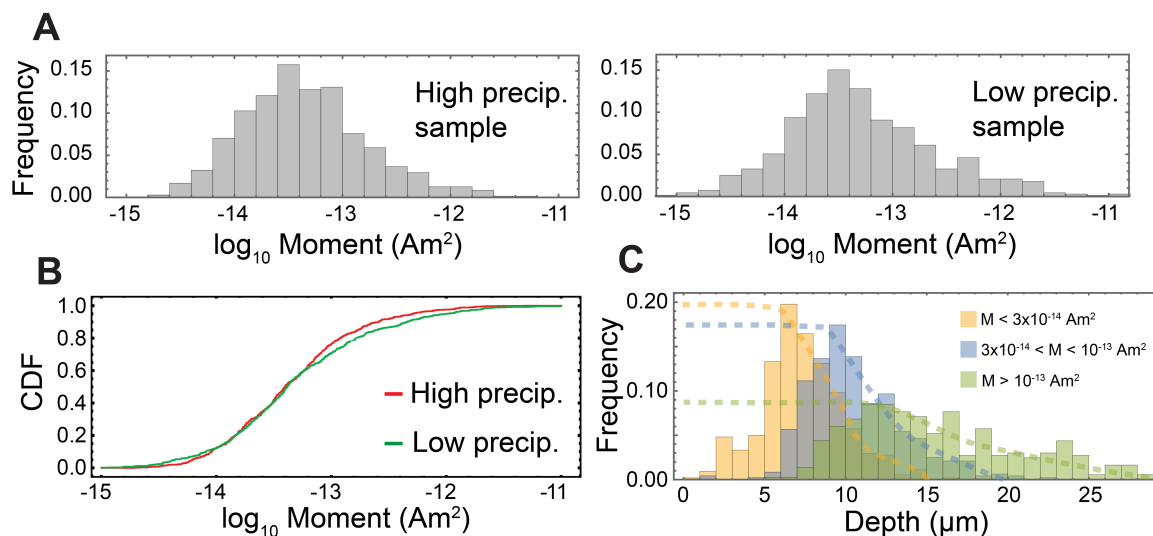


**Figure 2.** Single grain magnetizations for the coarse, individually resolved population of ferrimagnetic grains. (A) Distribution of magnetic moments for grains from the high- and low-precipitation samples. (B) Comparison of single grain magnetization distributions in the two soils displayed as a cumulative distribution function (CDF). A two-sample Kolmogorov-Smirnov test yields a  $p$  value of 0.13, implying insufficient evidence to demonstrate that the two populations have distinct distributions. (C) Distribution of depths of individual fitted sources separated by individual magnetic moments.

For QDM-based ARM experiments, we used a relatively high, 0.3 mT DC bias field to maximize the signal-to-noise ratio of magnet field maps. To quantify non-linearity in ARM acquisition, we imparted ARMs to bulk samples in 0.05 to 0.3 mT bias fields, finding that ARM intensities in a 0.3 mT bias field are 16% lower than expected from a linear extrapolation of lower bias field ARMs. We used this value to find the expected low-field ARM intensities before computing the ARM susceptibility. ARM bias fields and pulsed fields used in IRM acquisition were oriented to within  $2^\circ$  of the 12 o'clock, in-plane direction in all QDM maps.

After completing magnetic field imaging experiments, we carbon coated selected polished sections for analysis on a JEOL 7900F electron microscope at the Center for Nanoscale Systems at Harvard University. We used the backscattered electron (BSE) and Oxford Instruments energy dispersive spectroscopy (EDS) x-ray detectors to conduct high-resolution electron microscopy and elemental composition analysis. EDS data were quantified using Oxford Aztec software while quantification was performed using certified microanalysis standards for the measured elements and calibrated for the 5 keV beam energy.

## Results

### *Magnetic imaging of coarse magnetic population*

All QDM maps of ARM in the high and low-precipitation soils reveal abundant discrete remanence-carrying sources distributed throughout the sample volume (Fig. 1). We refer to these individually-resolved sources as the “coarse population” based on the high magnitude of individual magnetizations and electron microscopy showing them to be typically larger than several micrometers (see *Electron microscopy* Section below). To quantify the magnetization of each imaged grain, we fitted all isolated sources using a dipole model (Lima and Weiss, 2016; Fu et al., 2020), resulting in 672 and 711 fitted magnetic sources over a combined area of 57 and 41 mm<sup>2</sup> for the high- and low-precipitation samples, respectively. For both soils, the magnetic moment of individual coarse sources ranged between 10<sup>-15</sup> and 10<sup>-11</sup> Am<sup>2</sup> with a peak at approximately 3×10<sup>-14</sup> Am<sup>2</sup> (Fig. 2A).

To quantify the contribution of coarse sources to the total magnetization, we vector-summed the individual magnetizations and divided by the area and typical source depth, which is approximately 10 μm based on averaging the distribution of depths determined by net moment inversion (Fig. 2C). Sources at greater depths are progressively rarer due to the fall-off of their magnetic fields with distance. This analysis shows that the coarse magnetic sources contribute 4.5% and 40.6% of the bulk ARM for the high- and low-precipitation soils, respectively.

These percentages may underestimate the total coarse grain magnetization for several reasons. First, we binned pixels in 4×4 blocks to maximize signal-to-noise ratio for these ARM maps, resulting in a spatial resolution of 4.7 μm per pixel. Therefore, sources located fewer than a few μm from the surface would generate opposing magnetic fields that fall predominantly into a single pixel, preventing their identification. This effect produces the lack of fitted sources of any magnitude with less than ~3 μm depth (Fig. 2C). Second, because we only performed quantitative inversions on well-defined magnetic field signals, we excluded sources located in close proximity to neighboring ferrimagnetic particles, which results in highly non-dipolar magnetic field signatures (Fig. 1). This interference is more significant for stronger grains, which generate substantial magnetic field signal over a large volume and are therefore more likely to

interfere with neighboring sources. This effect accounts for the deficit of shallow and strongly magnetized grains among the sources in our compilation (Fig. 2C).

Regardless of the cause(s) of under-sampling, no physical mechanism can result in a true depletion of magnetic sources in the near surface given our randomly selected cut plane. We therefore estimate the contribution of missing shallow coarse magnetic sources by extrapolating the peak value of the depth histogram to the surface (dashed curves in Fig. 2C). This peak value is likely the best estimate for the true density of magnetic sources at a given depth, since recovered source concentrations are suppressed by magnetic field fall-off and by the near surface biases described above, respectively.

By this estimation, these missing sources appears to account for slightly over 50% of the total coarse source moment, implying that approximately 95% of the bulk magnetization in the low-precipitation soil can be attributed to coarse ferrimagnetic grains. This extrapolation is consistent with the lack of any other magnetic grain population, such as ultrafine particles (see below), observed in the low-precipitation soil. More advanced inversion techniques, including potential coupling to tomographic grain mapping (de Groot et al., 2021), can potentially result in the direct characterization of closer to 100% of resolvable magnetic sources in QDM maps.

Even without a complete inventory, the grain-level magnetization data on the coarse grains can be used to constrain their origin. Adopting a magnetite or maghemite composition, based on our electron microscopy results (see below), yields a diameter of 0.4, 1.0, and 10  $\mu\text{m}$  for weakly magnetized, modal, and strongly magnetized grains in this population assuming a saturation remanent magnetization to saturation magnetization ratio ( $M_{rs}/M_s$ ) of between 0.2 and 0.02 corresponding to the appropriate grain size (Roberts et al., 2017). These grain sizes are much larger than those reported for pedogenic and biogenic magnetite populations (Maher and Thompson, 1992; Nie et al., 2010). In fact, our electron microscopy of coarse grains (see below) shows that some grains associated with coarse magnetic signals are even larger, with diameters in the 10-30  $\mu\text{m}$  range. The  $\leq 10$   $\mu\text{m}$  equivalent diameter estimated from grain magnetizations may therefore represent ferrimagnetic sub-regions within the polymineralic grains. These 0.4 - 30  $\mu\text{m}$  ferrimagnet grain sizes are on the finer end of, but still overlap significantly with, those of other wind-blown loess deposits, which are dominated by 10-100  $\mu\text{m}$  diameter particles (Újvári et al., 2016). We therefore conclude that the discrete ferrimagnetic sources observed in both high- and low-precipitation soil samples are associated with the aeolian supply of coarse detrital magnetic grains.

We observe no significant difference between the distribution of the coarse population magnetic moment magnitudes of the low- and high-rainfall soils using a two sample Kolmogorov-Smirnov test ( $p = 0.13$ ; Fig. 2B). Further, the total magnetic moment of all resolved grains in each 3.15  $\text{mm}^2$  field of view is  $9.45 \pm 6.85 \times 10^{-12} \text{ Am}^2$  and  $6.82 \pm 2.68 \times 10^{-12} \text{ Am}^2$  ( $1\sigma$ ) for the high- and low-precipitation soils, respectively, again implying no resolvable difference between the two sites (Student's t-test  $p = 0.20$ ). Together, these

data demonstrate that the grain-level properties and the concentration of coarse-grained magnetic sources are indistinguishable at these high- and low-precipitation sites. This suggests that the coarse sources in both samples share the same detrital origin and that no additional magnetic enhancement occurred for this grain population at the higher rainfall locality.

#### *Magnetic imaging of ultrafine magnetic population in high-precipitation sample*

In contrast to the low-precipitation soil, the high-precipitation soil contains an additional population of unresolved, high-ARM susceptibility ( $k_{ARM}$ ) ferrimagnetic grains in addition to the above-described coarse ferrimagnetic grains. We hereafter referred to these grains as the “ultrafine” population. Although individual magnetic grains in this population are not resolvable in either QDM or optical images, diffuse positive and negative magnetic fields at the 12 o’clock and 6 o’clock edge of the sample are visible in the QDM maps for this high-precipitation soil (Fig. 1A, small black arrows). This magnetic field morphology indicates a net magnetization in the 12 o’clock direction, implying that the sample volume has acquired an ARM in the direction of the bias field. The consistent intensity of these fringing fields along the entire sample edge attests to the nearly uniform presence of this unresolved magnetic grain population throughout the volume of the high-precipitation soil. Notably, these fringing fields are not observed in the low-precipitation soil maps (Fig. 1B), implying that this ultrafine grain population is not measurably present in those samples.

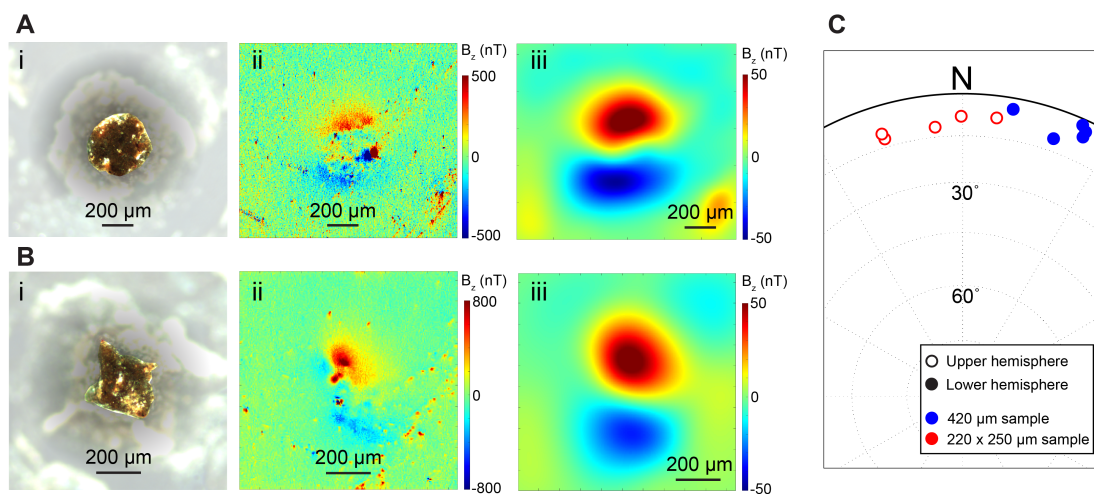


**Figure 3.** Net magnetic moment analysis of high-precipitation soil sub-volumes dominated by ultrafine grained magnetic carriers. Panels i through iii show, respectively, a reflected light, crossed polars photomicrograph, a raw QDM magnetic field map, and upward-continued and coarse source-subtracted magnetic field maps of the (A) 420  $\mu\text{m}$ -diameter and (B) 220 $\times$ 250  $\mu\text{m}$  sub-volumes. (C) Equal area stereonet projection of repeat ARM directions recovered from the two ultra-fine grain dominated sub-volumes. Bias field direction for all ARMs is due north with zero inclination.

We can use the QDM data to characterize the concentration, coercivity spectrum, and grain size distribution of this ultrafine ferrimagnetic grain population. We first used non-magnetic tools to isolate a 300  $\mu\text{m}$  thick, 420  $\mu\text{m}$ -diameter sub-volume of the high-precipitation sample relatively free from coarse magnetic sources (Fig. 3). We refer to this specimen hereafter as the “ultrafine grain sub-volume”. Next, we imparted a 300 mT AC field and 0.3 mT DC field ARM followed by stepwise AF demagnetization in 2.5 to 5 mT steps up to 40 mT, by which point the direction of magnetization was fully randomized. We subtracted the fitted dipole signal arising from a coarse magnetic particle and fitted for the net magnetic moment of the remaining signal after 120  $\mu\text{m}$  upward continuation using a dipole model after each ARM or AF application (Fu et al., 2020). Further, we measured the magnetization of this sub-volume after imparting a 0.3 T IRM. As evidenced by the AF demagnetization sequence (Fig. 4), the soft coercivity of the ultrafine grain sub-volume implies that this low DC field value is able to produce a near-saturation IRM.

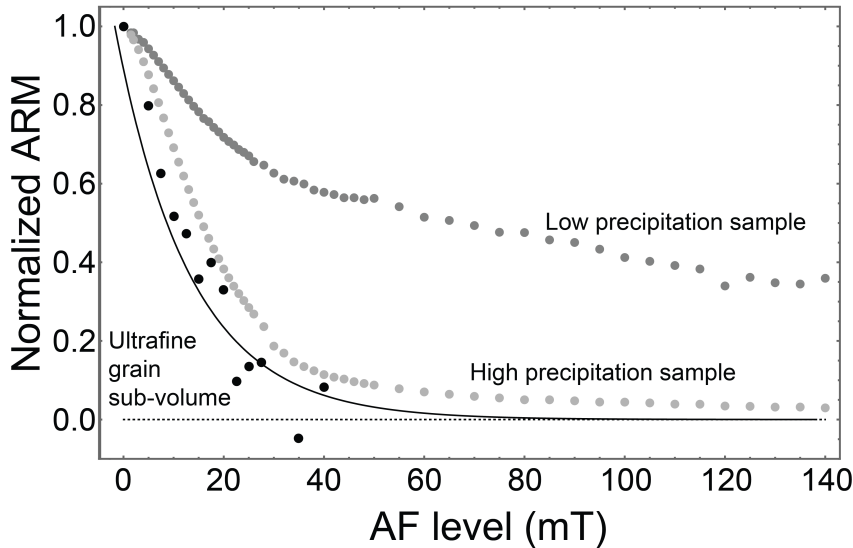


**Figure 4.** AF demagnetization of ARM for high- and low-precipitation bulk samples and the ultrafine grain sub-volume. Black solid line shows the best-fit exponential curve for the ultrafine grain sub-volume data. Plotted magnetization is the projection of the measured vector magnetization in the ARM bias field direction.

We first quantify the contribution of the ultrafine ferrimagnetic grain population to the total magnetization. By normalizing the ultrafine sub-volume ARM moment to its volume and comparing it to the ARM intensity of the bulk sample, we find that the ultrafine population can account for  $88 \pm 8\%$  ( $1\sigma$ ) of the total sample ARM, where the uncertainty is based on the reproducibility of the ARM.

Combining this value with the 4.5% of ARM contributed by the coarse grain population in the high-precipitation sample results in  $\sim 93\%$  of the measured bulk

magnetization. Adopting the low-precipitation sample as a guide, individually quantifiable coarse grain magnetic sources account for 40% of the total magnetization while the remaining 60% likely arises from additional coarse grain sources that could not be sufficiently isolated (see discussion above). Therefore, the total contribution of coarse grains in the high-precipitation soil is likely  $\sim 11\%$ , bringing the ultrafine plus coarse grain magnetization in the high-precipitation soil very close to 100%. This consistency both indicates that no other significant ferrimagnetic grain population is present in the high-precipitation soil and corroborates the estimated 40:60 ratio of individually quantified to not individually quantified coarse grain sources estimated above.

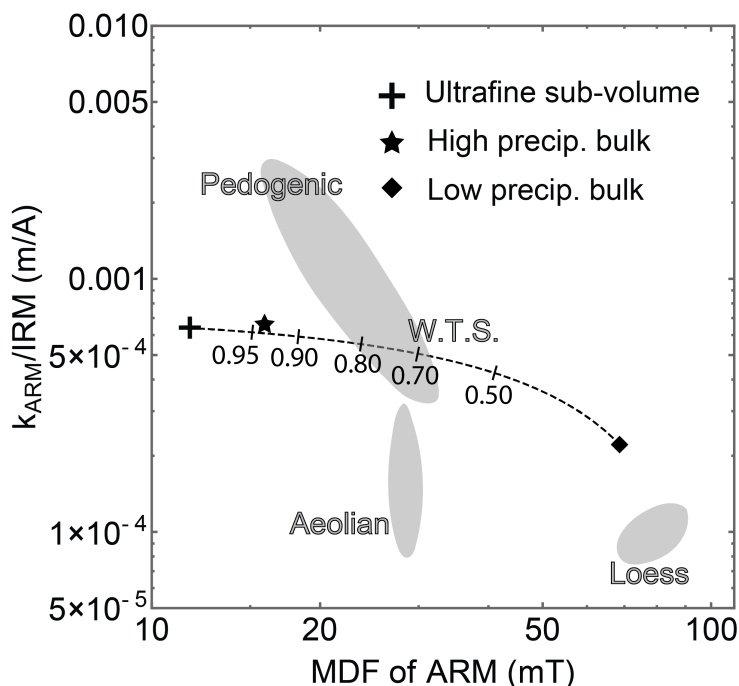


**Figure 5.** Coercivity and IRM-normalized ARM susceptibility of the ultrafine sub-volume and of the high- and low-precipitation bulk soils. Dashed curve indicates a linear mixing curve between the ultrafine and low-precipitation bulk endmembers with the number indicating volume fraction of the ultrafine grain population. Gray regions and labels are from compilation study by Egli (2004). W.T.S. denotes water transported sediments, including fluvial and proglacial environments.

Second, we characterized the magnetic properties of the ultrafine population using a combination of ARM demagnetization and IRM acquisition. Using QDM data from the  $420\ \mu\text{m}$ -diameter ultrafine grain sub-volume, we computed the IRM-normalized ARM susceptibility ( $k_{ARM}/IRM$ ) and mean destructive field of ARM ( $MDF$ ; Fig. 4). Together, these two parameters are a well-studied, albeit non-unique, proxy for magnetite grain size and origin with ultrafine fine, pedogenic magnetites typically showing high  $k_{ARM}$

and low  $MDF$  (Maher, 1988; Egli, 2004). Our analyses show that the ultrafine ferrimagnetic grains fall near the region encompassed by pedogenic magnetite, although with lower ARM susceptibility ( $\frac{k_{ARM}}{IRM} = 6.4 \times 10^{-4} \text{ m A}^{-1}$ ;  $MDF_{ARM} = 11.7 \text{ mT}$ ; Fig. 5). For comparison, the high-precipitation bulk soil sample revealed moderately higher coercivity and similar ARM susceptibility, although still corresponding to pedogenic magnetite ( $\frac{k_{ARM}}{IRM} = 6.7 \times 10^{-4} \text{ m A}^{-1}$ ;  $MDF_{ARM} = 15.9 \text{ mT}$ ).

As presented earlier, the analysis of ARM intensities contributed by the ultrafine and coarse grain populations within the high-precipitation soil implies that the bulk  $k_{ARM}/IRM$  and  $MDF_{ARM}$  parameters should represent a linear combination of ultrafine and coarse grain signal with the former population dominating. A bulk sample from the low-precipitation locality, which appears to contain only coarse grain-hosted magnetization in QDM maps, displays magnetic properties corresponding to a typical, weakly magnetized, highly oxidized loess deposit ( $\frac{k_{ARM}}{IRM} = 2.2 \times 10^{-4} \text{ m A}^{-1}$ ;  $MDF_{ARM} = 68.7 \text{ mT}$ ; Fig. 5). Adopting these properties for the coarse-grained endmember, a linear mixing model shows that the bulk  $k_{ARM}/IRM$  and  $MDF_{ARM}$  of the high-precipitation sample is best explained by a 94% to 6% mixture of ultrafine and coarse grain components by volume, respectively. This proportion is within uncertainty of the  $88 \pm 8\%$  by volume estimate derived earlier from ARM intensity and confirms that the magnetization of the high-precipitation sample is dominated by the ultrafine grain population.

In summary, these concordant estimates based on ARM intensity and on  $k_{ARM}/IRM$  and  $MDF$  values provide further evidence for, first, the similarity of the coarse ferrimagnetic grain population in the two soils and, second, the presence of an additional, magnetically dominant ultra-fine grain population in the high-precipitation soil. Further, these analyses show that QDM imaging is able to separately characterize the rock magnetic properties from two distinct, intimately mixed grain populations that, together, account for approximately 100% of ferromagnetic material.

#### *Grain size estimation from precision of ARM acquisition*

The QDM's ability to measure an ARM signal from small sample volumes potentially provides a novel means for quantifying characteristic ferromagnetic grain size. The fidelity with which a sample can record the direction of an imparted thermoremanent magnetization (TRM) increases with the number of individual ferromagnetic grains present (Berndt et al., 2016). For centimeter-scale core samples containing  $\gg 10^7$  ferromagnetic grains, this statistical uncertainty is a fraction of a degree and cannot be easily quantified using typical rock magnetic measurements.

However, if isolated soil sub-volumes imaged using the QDM contain sufficiently few ferromagnetic grains on the order of  $10^5$  to  $10^6$ , this statistical scatter may range between  $1^\circ$  to  $>10^\circ$ . In comparison, optical images taken with every QDM experiment permits sample placement repeatability of  $\sim 1^\circ$ . Reproducibility of the sample mounting

orientation with respect to the ARM bias field coil is also  $<1^\circ$ . We therefore attempted to quantify the amplitude of random variations in the acquired ARM direction to estimate the number of ferromagnetic grains contained. Due to greater uncertainties associated with net moment inversions of the magnetization magnitude (Fu et al., 2020), we limited our analysis to the recovered ARM directions. Further, we focused on the distribution in ARM declination by applying an average field value subtraction, which decreases the spread of the fitted direction in inclination (Fig. 3C). Dipole inversions of declination are typically more accurate than that of inclination while, assuming isotropic sources, the variance in declination alone should provide full information on ARM reproducibility (Maxwell and Garrick-Bethell, 2020).

Importantly, applying the TRM analysis from Berndt et al. (2016) to ARM data requires an ARM acquisition process that maximizes thermally activated grain behavior. We find that ramping down the AC field at slow rates of  $1 \text{ mT s}^{-1}$  provides sufficient opportunities for thermally activated grain remagnetization that nearly all grain smaller than 140 nm would nearly reach thermal equilibrium (Supplemental Materials). Due to heat dissipation limitations on the AF coil, we were limited to a peak AF level of 50 mT for such slow ramp downs, which is sufficiently strong given the low coercivities (11.7 mT; see above) of the ultrafine magnetic sources. In total, we imparted six repeated, identical ARMs with 50 mT AC and 0.3 mT DC magnetic fields to the 420  $\mu\text{m}$ -diameter ultrafine grain sub-volume and obtained QDM magnetic field maps and net moment inversions after each ARM application.

Compilation of these fitted directions shows that the ultrafine-grained sub-volume is capable of reproducing the applied ARM direction with an angular standard deviation of  $6.2^\circ$  (Fig. 3). This level of scatter corresponds to between  $6.1 \times 10^6$  and  $9.2 \times 10^7$  discrete particles, depending on whether an empirical ARM to TRM efficiency factor of  $\sim 3.9$  is included in determining the effective bias field (Yu, 2010). Given a measured IRM of  $4.9 \times 10^{-10} \text{ Am}^2$  and a characteristic  $M_{rs}/M_s$  value for pedogenically enhanced soil of 0.15, this range of particle counts corresponds to average particle diameters of between 48 and 140 nm, assuming spherical magnetite grains. Repeating this experiment on a second,  $220 \times 250 \mu\text{m}$  sub-volume of ultrafine-grained material yields comparable estimates of 51 to 150 nm diameter grains.

These values are likely to overestimate the true typical single grain sizes because the occurrence of ferrimagnetic particles in clusters, as suggested by our electron microscopy results (see below), would partially attenuate the applied bias field through magnetostatic interactions with the backfields of neighboring particles. The degree of ARM alignment to the bias field direction would therefore be less precise in the case of clustered particles, implying that a greater number of particles would be required to achieve a given level of precision. This greater number of particles would then correspond to smaller magnetic moments and diameters for each particle. In any case, the inferred particle diameters from this analysis are significantly smaller than those

expected for windblown loess grains and directly imaged detrital grain sizes belonging to the coarse ferrimagnet population [see below; (Újvári et al., 2016)], implying a non-detrital origin for the ultrafine grain population.

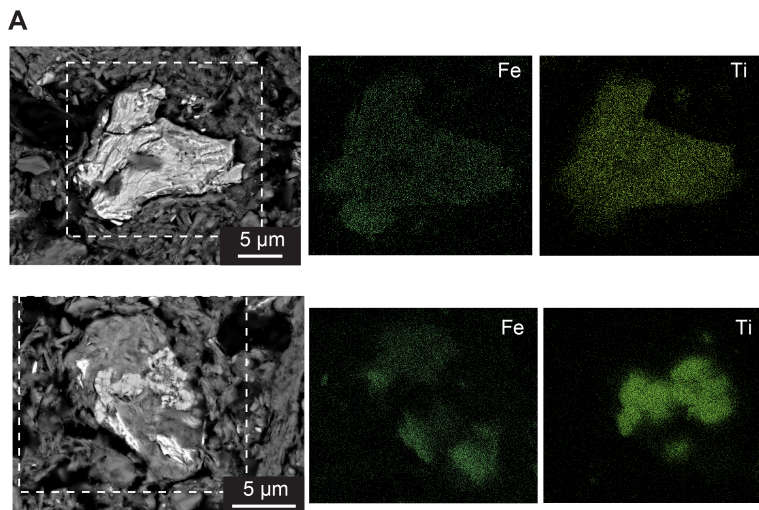


**Figure 6.** Scanning electron microscopy of coarse ferrimagnetic sources in the high-precipitation sample. The grains correspond to the labeled magnetic field sources in Fig. 2A. Left column is the BSE overview image while right columns show the distribution of Fe and Ti as detected using EDS x-ray spectroscopy.

#### *Electron microscopy*

Our rock magnetic and magnetic imaging analyses described above demonstrate the presence of two classes of ferrimagnetic grains in Qilianshan soils: a population of 0.4 - 10  $\mu\text{m}$ , coarse Fe-oxides occurring with similar concentrations in both high- and low-precipitation samples; and a population of  $\leq 150$  nm diameter grains that occur only in the high-precipitation soil. We pursued high-resolution SEM imaging and EDS analyses to image these two different ferrimagnetic grain populations and quantify their chemical composition.

For the coarse grain population, we can use QDM mapping to locate individual remanence-carrying grains for SEM and EDS analyses (Fig. 6). BSE imaging of these sources in the high-precipitation sample reveals that that the host grains are typically 1-30  $\mu\text{m}$  Fe,Ti-oxides with variable Fe to Ti ratio. The size and angular morphology of these grains support an aeolian origin, which is consistent with rock magnetic characterization discussed above (Vandenberghé et al., 1997; Újvári et al., 2016).

For the ultrafine grain population, neither QDM nor optical imaging have sufficiently high resolution to isolate individual grains. We therefore first used QDM maps of a vertically-oriented, 300 mT IRM to locate the highest concentration of ferromagnetic

grains within 420  $\mu\text{m}$ -diameter ultrafine grain sub-volume. We then defined a 170 $\times$ 140  $\mu\text{m}$  region encompassing the strongest magnetic fields (Fig. 7).

Systematic survey of this region in BSE imaging mode at high magnification revealed the presence of clusters of 10s to 100s nm diameter, high atomic number ( $z$ ) grains, hereafter referred to as “ultrafine high- $z$ ” particles (Fig. 7B,C). Individual ultrafine high- $z$  grains are too small for quantitative analysis using the electron microprobe due to the longer length scale of the electron beam’s interaction volume, which results in severe mixing of characteristic x-rays from the surrounding silicates. However, given our operation at low,  $\leq 5$  keV acceleration voltages, the 1-3  $\mu\text{m}$  diameter of some clusters is significantly larger than the  $\sim 400$  nm expected interaction depth of the electron beam as estimated from Monte Carlo simulations using the CASINO v2.5.1 software (Drouin et al., 2007).

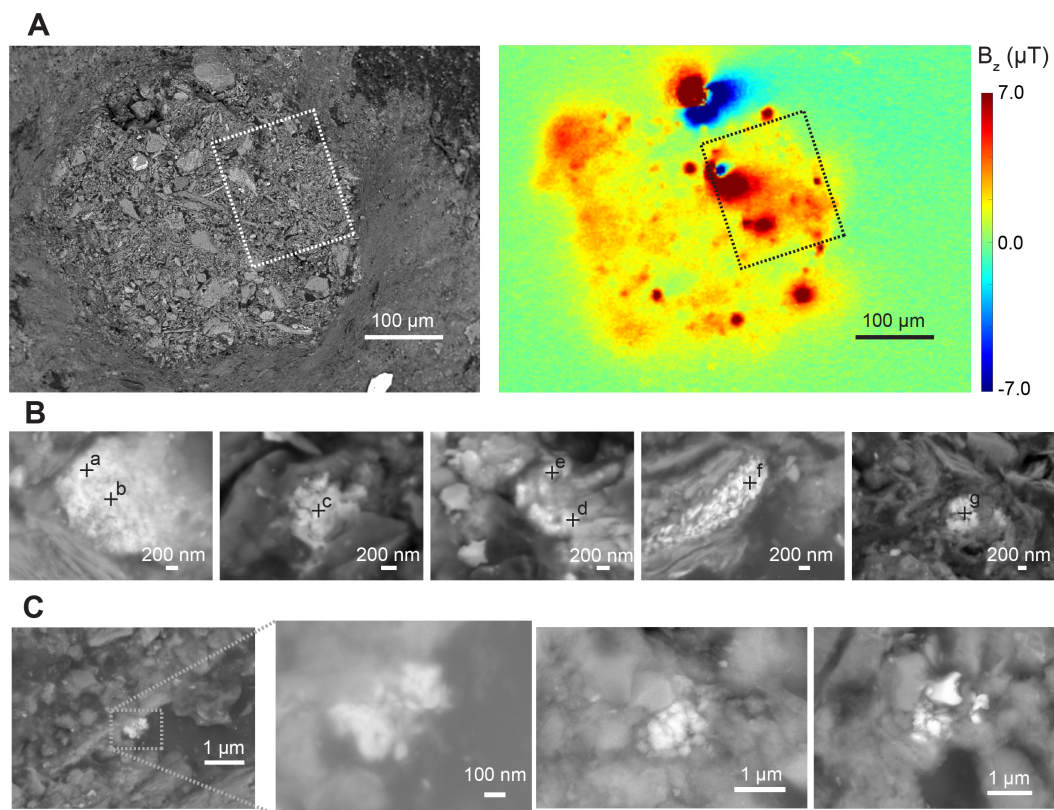


**Figure 7.** Scanning electron microscopy of ultrafine ferrimagnetic sources in the high-precipitation sample. (A) BSE map and QDM magnetic field map of the same field of view covering the  $\sim 420$   $\mu\text{m}$ -diameter ultrafine grain sub-volume. Dashed rectangle denotes the sub-region in which we looked for high- $z$  particles at high resolution using the SEM. The sample was given a 0.3 T IRM in the out-of-plane direction prior to QDM mapping. Red and blue colors correspond to out-of-plane and into-plane magnetic fields, respectively. (B) High magnification images of ferrimagnetic sources. Locations labeled a through g correspond to the sites of EDS elemental composition analysis (Table 1). (C) Additional high- $z$  particles detected in the searched region.

We therefore acquired EDS spectra of five ultrafine high-z clusters in conjunction with immediately adjacent silicates using a 5 keV acceleration voltage (Table 1). Even with the low beam interaction volume, all analyses included a minor contribution from silicates with Si content between 1.8 and 7.6 wt% with most values below 2.8%. We interpreted this component as due to mixing of characteristic x-rays from surrounding silicates and subtracted off the composition of the adjacent silicates weighted such that resulting background-subtract composition has zero Si. With this correction, the concentrations of two other silicate-forming elements, Al and Mg, both converged closer to zero for all analyses, providing support for the validity of the silicate background subtraction step. The total recovered wt% for the pre-subtracted and silicate background analyses suggest an analytical precision of ~5 wt%

We then computed the Fe:O ratio for all high-z grain clusters, finding a wide range between 0.72 and 1.19 with most values below 0.81 (Table 1). Comparing these ratios to those expected for magnetite (Fe:O = 0.75) and hematite and maghemite (Fe:O = 0.67), we find that two out of seven analyses were within uncertainty of either Fe-oxide composition. Meanwhile, three out of the seven were compatible with only magnetite while the remaining two analyses showed higher Fe:O ratios suggesting the presence of unsubtracted Fe<sup>2+</sup>, likely in silicate phases. All analyses contained Fe:O ratios closer to magnetite than hematite or maghemite. In contrast to coarse ferrimagnetic grains associated resolved magnetic sources (Fig. 6), no analyzed ultrafine high-z grain clusters contained any resolvable Ti enrichment.

## Discussion

Our joint QDM magnetic field imaging and electron microscopy analyses hold implications for understanding the mechanism of magnetic enhancement in a modern, loess-derived soil and, more generally, for establishing a new methodology for determining the mechanism of magnetic enhancement.

Multiple mechanisms have been proposed to explain well-established correlations between precipitation and soil magnetic properties. Specifically, past studies have documented, among other changes, enhanced total ferrimagnetic content, higher ARM susceptibility, and reduced mean coercivity in well-buffered soils from high-precipitation localities [e.g., Maher et al. (1994); Geiss et al. (2008); Balsam et al. (2011); Sharifigarmdareh et al. (2020); see Maxbauer et al. (2016) for review].

Bulk rock magnetic characterization of our Qilianshan soils confirm these general relationships with the higher-precipitation, low-temperature sample displaying enhanced saturation remanent magnetization, higher  $k_{ARM}/IRM$ , and lower  $MDF$  compared to the low-precipitation, high-temperature specimen (Fig. 5; Table 1). Although these bulk sample observations suggest an influence of precipitation on magnetic properties, they cannot uniquely identify the mechanism(s) producing the contrasting magnetic behaviors. As reviewed in the Introduction, these proposed

magnetic enhancement mechanisms have included compaction, changes in the detrital input, and *in situ* formation of ferrimagnets resulting from alteration of existing Fe-bearing phases or precipitation in soil pore spaces during wet and dry cycling.

QDM magnetic field imaging can aid in identifying the dominant magnetic enhancement mechanism in Qilianshan soils. QDM maps show that both high- and low-precipitation soils contain an indistinguishable population of QDM-resolvable, coarse ferrimagnetic grains with  $\sim 1 - 30 \mu\text{m}$  diameter based on both magnetic moment inversions and electron microscopy (Figs. 2, 6). The grain size distribution and Ti-composition of these grains strongly suggest a detrital origin. These observations show that any differences in deposition rate or in the composition of the aeolian input or *in situ* magnetic enhancement of coarse, detrital Fe-oxide particles do not contribute significantly to the contrasting magnetic properties of the high- and low-precipitation soils.

In contrast, QDM mapping reveals that the high-precipitation soil can acquire a strong, uniform ARM throughout the sample volume, providing evidence for an additional population of ultrafine ferromagnetic particles (Figs. 1, 3). This grain population accounts for  $88 \pm 8\%$  of the total high-precipitation sample ARM, suggesting that the formation of these ultrafine particles alone explains the  $\sim 11\times$  enhancement in  $k_{ARM}$  between the low- and high-precipitation bulk samples. Further, the fact that the proportion of ultrafine grain-carried magnetization as computed from magnetization intensity ( $\sim 88\%$ ) and from a mixing model based on  $k_{ARM}/IRM$  and  $MDF$  parameters ( $\sim 94\%$ ) are consistent within uncertainty implies that this same grain population is responsible for all observed magnetic enhancement, including the increased total magnetization, ARM susceptibility, and coercivity changes.

The relatively high  $k_{ARM}/IRM$  and very soft  $MDF$  parameters for this ultrafine population is consistent with a pedogenic origin based on comparison with previously studied modern and ancient soils, although with lower than typical  $k_{ARM}/IRM$ . Further, ARM reproducibility-based estimates of individual ultrafine grain volumes yielded individual grain diameters between  $\sim 50$  and  $140 \text{ nm}$ , which are significantly smaller than even very fine aeolian particles (Újvári et al., 2016). Together, these magnetic observations provide strong evidence that magnetic changes in the high-precipitation soil resulted from the *in situ* formation of this ultrafine ferrimagnetic particle population.

QDM data can further be used to identify the formation pathway of this ultrafine grain population. Magnetic field maps of ARM demonstrates that ultrafine grains occur uniformly throughout the high-precipitation soil with no locational relationship to coarser Fe-oxide or silicate grains (Figs. 1, 3). These authigenic ferrimagnets are therefore very unlikely to have altered directly from Fe within these reservoirs.

At the same time, the magnetic field maps allow us to identify regions that lack coarse ferrimagnetic grains while carrying strong ultrafine grain-hosted magnetization. Our SEM survey of one such region revealed  $\sim 10\text{-}300 \text{ nm}$  diameter, high-atomic number

grains that occur in micrometer-scale clusters (Fig. 7). These grains, which have diameters that overlap strongly with the size range inferred from the ARM reproducibility analysis described above, contain undetectable Ti concentrations, further demonstrating an origin independent of Ti-rich ferromagnetic grains associated with coarse magnetic field sources (Fig. 6). Previous studies have similarly demonstrated an absence of substitution by Ti or Al in pedogenic ferrites (Maher and Thompson, 1992; Ahmed and Maher, 2018).

Having identified the physical sites of magnetic enhancement, we can use EDS-derived elemental compositions to constrain the chemical pathway leading to pedogenic Fe-oxide grain formation. As discussed in the Introduction, two distinct reaction series can result in the precipitation of magnetite or maghemite from soil pore fluids, thereby accounting for the uniform occurrence of Fe-oxide grain clusters throughout the soil volume. These two mechanisms make distinct predictions for the oxidation state of pedogenic ferrimagnets. Specifically, the wet and dry cycling hypothesis predicts direct formation of  $\text{Fe}_3\text{O}_4$  (magnetite), some of which may be subsequently oxidized to  $\gamma\text{-Fe}_2\text{O}_3$  (maghemite) (Maher and Thompson, 1992; Maher, 1998; Orgeira et al., 2011; Ahmed and Maher, 2018). On the other hand, the ferrihydrite  $\rightarrow$  maghemite  $\rightarrow$  hematite transformation mechanism requires that Fe occurs in the  $\text{Fe}^{3+}$  form only during the magnetic enhancement process (Torrent et al., 2007).

Our measured Fe:O ratios for the ultrafine Fe-oxide clusters show that all imaged Fe-oxides are more consistent with the magnetite ratio of 3:4, although two out of seven clusters are within uncertainty of the 2:3 maghemite ratio (Table 1). Therefore, although we cannot rule out some contribution to the total magnetization from maghemite sources, the bulk of the ultrafine Fe-oxide population has a mixed  $\text{Fe}^{2+}$  and  $\text{Fe}^{3+}$  composition, supporting an origin during wet and dry cycling, with mobilization of  $\text{Fe}^{2+}$  in temporarily reducing conditions and its partial oxidation and precipitation upon subsequent drying and re-oxidation of soil micro-environments (Maher and Thompson, 1992).

An additional distinguishing characteristic between these two mechanisms of pedogenic ferrimagnet formation is the presence of Al substitution in the Fe-oxide phases, which is expected for the ferrihydrite  $\rightarrow$  maghemite  $\rightarrow$  hematite pathway. Specifically, visible diffuse reflectance spectrum measurements have been used on CLP paleosols to show that pedogenic hematite has lower  $P_{560}$  values between ~530 and 545 nm (Hu et al., 2013). This parameter, which quantifies the shift in an electron transition energy as inferred from changes in the reflectance spectrum, has been measured for a range of synthetic, Al-substituted hematites (Kosmas, 1986; Liu et al., 2011). These calibration studies have measured  $P_{560}$  values below 545 nm only in samples with at least 4 molar percent (mol%; equivalent to 3.3 wt% for an  $\text{Fe}_2\text{O}_3$  composition) Al substitution, with most samples in the  $P_{560} = 530\text{-}545$  containing 5-13 mol% (4.1-10.8 wt%) Al. No Fe-oxide clusters from our EDS analyses contain greater than 3.5 mol%, while the two Fe-oxide clusters from our analyses that have Fe:O ratio compatible with  $\text{Fe}_2\text{O}_3$  have a

maximum Al content of only 2.7 wt% (Table 1). The uncertainties on these measured Al contents are likely on the order of several percent, preventing us from conclusively excluding larger Al enrichments. Nevertheless, these low Al contents are most compatible with a magnetite-forming pathway, which specifically precludes Al substitution (Taylor et al., 1986).

In terms of rock magnetism techniques, our study demonstrates several novel uses of high-resolution magnetic field imaging. First, we have shown that QDM magnetic field imaging is capable of accurately quantifying remanence-based rock magnetic parameters such as remanent magnetization intensity, remanence susceptibility, and remanence coercivity directly from individual magnetic grain populations, even if distinct grains types are intimately mixed. In the case of our high-precipitation soil, QDM measurements provided the  $k_{ARM}/IRM$  and AF demagnetization spectra of ultrafine ferrimagnetic grains after numerical subtraction of confounding coarse grained sources. The location of this ultrafine grain population in  $k_{ARM}/IRM - MDF$  space on a mixing curve determined from bulk sample measurements confirms the accuracy of these recovered parameters (Fig. 5).

Second, our analysis of the coarse ferrimagnetic grain population shows that quantitative net moment inversion, applied over several hundred sources, can generate a statistically meaningful representation of individual grain moment and estimated diameter distributions. This information can be used to characterize directly magnetic differences in aeolian precursor grains and to document any magnetic enhancement within this population. The QDM can therefore serve as a rapid method for assessing changes in rock magnetic properties arising from provenance variations or coarse Fe-oxide alteration rather than from authigenic ferrimagnets. Establishing the relative magnitudes of detrital and pedogenic contributions is key to determining whether climofunctions based on the growth of ultrafine ferrimagnets can be reliably applied. This capability may be especially important to study areas with less well-established evidence for a high degree of aeolian grain mixing and uniformity compared to the CLP (Maher et al., 2009).

Third, QDM magnetic field maps can reveal potential spatial associations between magnetic sources and, for example, other Fe-bearing phases from which they are altered. In the case of Qilianshan soils, the lack of correlation between ultrafine grains and detrital Fe-bearing phases and the disseminated distribution of ultrafine grains provide evidence for pore space ferrimagnet precipitation. Imaging of magnetic particles locations also enables follow-up analysis using, for example, electron microscopy to quantify grain size and composition.

Finally, we have isolated sufficiently small volumes of ferromagnetic carriers such that the statistical uncertainty in reproducing a laboratory ARM can be used as a direct estimator of grain number density and, therefore, grain size. Future work potentially

involving micromagnetic modeling of interactions can potentially further exploit this data type to characterize the size and spatial distribution of unresolved grains.

## Conclusions

Our investigation into a pair of high- and low-rainfall soils from the Qilianshan Range was designed to evaluate the contribution of different proposed mechanisms to bulk soil magnetic enhancement and resultant rock magnetic changes. We developed and applied several high-resolution magnetic field imaging techniques to isolate the signal from distinct ferrimagnetic grain populations within the soil samples. This analysis led to the identification of two distinct ferrimagnetic particle populations. First, a coarse, 1-30  $\mu\text{m}$  diameter population of Fe-oxide and Fe,Ti-oxide grains are present in both soil types, carrying  $\sim 10\%$  and  $\sim 100\%$  of the total ARM in the high- and low-precipitation samples, respectively. The grain size and angular morphology of these coarse grains suggest an aeolian origin, while the lack of differences in the concentration and single-grain magnetization distributions between the two different soils indicate the lack of any climate-related magnetic changes within these grains.

Second, an ultrafine population of ferrimagnetic particles is present only at the high-precipitation locality and constitutes  $\sim 90\%$  of the total sample ARM. This population occurs throughout the entire sample volume, unrelated to the location of detrital magnetic grains, and exhibits high  $k_{ARM}/IRM$  ratio and soft coercivity compared to the aeolian ferrimagnetic grains. These traits are hallmarks of magnetically enhanced soils. EDS compositional measurements indicate a magnetite composition, strongly suggest that these grains formed during wet and dry cycling causing  $\text{Fe}^{2+}$  mobilization and subsequent precipitation of magnetite.

The pervasive presence of ultrafine magnetite grains in the higher precipitation soil is consistent with similar findings based on bulk sample rock magnetic analysis and electron microscopy studies (Maher and Thompson, 1991, 1992; Evans and Heller, 1994; Ahmed and Maher, 2018). Magnetic field imaging augments this picture in several ways. First, quantifying the magnetization of individual coarse ferrimagnetic grains permits the direct inference that the aeolian grain population has indistinguishable rock magnetic properties in the two localities and, therefore, that these grains did not participate in moisture-driven magnetic enhancement. Second, the sub-uniform distribution of the ultrafine grains confirms that, at least in these studied samples, pedogenic enhancement occurred throughout the sample volume and was not associated with precursor Fe-bearing silicates or oxides. Finally, magnetic imaging provides a framework for linking further non-magnetic characterization, such as electron microscopy, to specific magnetic grain populations.

Together, these insights provide strong constraints on the mechanism of magnetic enhancement in Qilianshan soils, demonstrating a set of methods that can potentially be

widely applied to paleosol and loess samples to determine the pathway of magnetic enhancement and verify the applicability of quantitative paleorainfall reconstructions.

### **Acknowledgements**

We thank M.W.R. Volk for discussions that improved the manuscript. RRF was funded by grants from the National Science Foundation (AGS-2202772) and the Lemann Brazil Fund.

### **Open Research**

Data Availability Statement: Data types for this work consist of QDM magnetic field maps, text files of net magnetization fitting results, bulk soil sample data from the 2G superconducting rock magnetometer, and SEM microscopy images and compositional maps. All data is publicly available on the Harvard Dataverse archive (Fu et al., 2022).

**Table 1: Background-subtracted EDS compositions of ultrafine high-z clusters**

Point ID	O	Na	Mg	Al	S	Ca	Ti	Fe	Si (Pre-subtraction)	High-z Point Total	Bkg. Point Total	Fe:O Atomic Ratio
a	26.9	0.1	0.5	0.6	0.21	0.7	0.0	70.5	1.8	106.8	95.9	0.75
b	23.9	0.1	0.5	0.6	0.18	0.8	0.0	59.9	2.4	95.6	95.9	0.72
c	25.1	0.2	0.6	3.5	0.0	0.0	0.0	71.3	2.2	105.7	87.2	0.81
d	21.5	0.0	0.9	2.2	0.0	1.3	0.0	58.6	4.6	106.7	87.1	0.78
e	14.9	0.1	0.1	2.7	0.2	4.0	0.0	37.3	7.6	94.9	87.1	0.72
f	22.3	0.1	0.0	0.0	0.0	0.0	0.0	71.2	1.6	104.9	94.8	0.92
g	14.9	0.0	0.2	0.0	0.0	0.7	0.0	61.2	3.7	99.4	96.4	1.18

Notes: All values except for Fe:O ratio are given in weight percent (wt%). Elemental columns give the composition of each high-z point after subtraction of silicate background assuming the high-z clusters do not contain Si. The “Si (Pre-subtraction)” column gives the wt% of Si in the original high-z cluster measurement. The two “Total” columns provide the total wt% of the high-z and surrounding silicate analyses. These three columns are designed to constrain the precision of the background-subtracted composition. The “Fe:O Atomic Ratio” column is computed from the background-subtracted elemental concentrations. For comparison, the Fe:O atomic ratios of stoichiometric magnetite, hematite, and maghemite are 0.75, 0.67, and 0.67, respectively.

## References

- Ahmed, I.A.M., and Maher, B.A., 2018, Identification and paleoclimatic significance of magnetite nanoparticles in soils: *Proceedings of the National Academy of Sciences*, v. 115, p. 1736–1741, doi:10.1073/pnas.1719186115.
- Balsam, W.L., Ellwood, B.B., Ji, J., Williams, E.R., Long, X., and El Hassani, A., 2011, Magnetic susceptibility as a proxy for rainfall: Worldwide data from tropical and temperate climate: *Quaternary Science Reviews*, v. 30, p. 2732–2744, doi:10.1016/j.quascirev.2011.06.002.
- Berndt, T., Muxworthy, A.R., and Fabian, K., 2016, Does size matter? Statistical limits of paleomagnetic field reconstruction from small rock specimens: *J. Geophys. Res. Solid Earth*, v. 121, p. 15–26, doi:10.1002/2015JB012441.
- Chen, T., Xu, H., Xie, Q., Chen, J., Ji, J., and Lu, H., 2005, Characteristics and genesis of maghemite in Chinese loess and paleosols: Mechanism for magnetic susceptibility enhancement in paleosols: *Earth Planet. Sci. Lett.*, v. 240, p. 790–802, doi:10.1016/j.epsl.2005.09.026.
- Drouin, D., Couture, A., Joly, D., Tastet, X., Aimez, V., and Gauvin, R., 2007, CASINO V2.42—A Fast and Easy-to-use Modeling Tool for Scanning Electron Microscopy and Microanalysis Users: *Scanning*, v. 29.
- Egli, R., 2004, Characterization of individual rock magnetic components by analysis of remanence curves: 1. Unmixing natural sediments: *Stud. Geophys. Geod.*, v. 48, p. 391–446.
- Evans, M.E., and Heller, F., 1994, Magnetic Enhancement and Palaeoclimate: Study of A Loess/Palaeosol Couplet Across the Loess Plateau of China: *Geophys. J. Int.*, v. 117, p. 257–264, doi:10.1111/j.1365-246X.1994.tb03316.x.
- Fu, R.R., Lima, E.A., Volk, M.W.R., and Trubko, R., 2020, High sensitivity moment magnetometry with the quantum diamond microscope: *Geochem. Geophys. Geosyst.*, v. 21, p. e2020GC009147.
- Fu, R.R., Maher, B.A., Nie, J., Gao, P., Berndt, T., and Cavanaugh, T., 2022, Replication Data for: Pinpointing the mechanism of magnetic enhancement in modern soils using high-resolution magnetic field imaging: <https://doi.org/10.7910/DVN/Z4CBN8>.
- Gao, P., Nie, J., Yan, Q., Zhang, X., Liu, Q., Cao, B., and Pan, B., 2021, Millennial Resolution Late Miocene Northern China Precipitation Record Spanning Astronomical Analogue Interval to the Future: *Geophysical Research Letters*, v. 48, doi:10.1029/2021GL093942.
- Geiss, C.E., Egli, R., and Zanner, W., 2008, Direct estimates of pedogenic magnetite as a tool to reconstruct past climates from buried soils: *J. Geophys. Res.*, v. 113, p. B11102.

- Glenn, D.R., Fu, R.R., Kehayias, P., Le Sage, D., Lima, E.A., Weiss, B.P., and Walsworth, R.L., 2017, Micrometer-scale magnetic imaging of geological samples using a quantum diamond microscope: *Geochemistry, Geophysics, Geosystems*, v. 18, p. 2017GC006946, doi:10.1002/2017GC006946.
- Groot, L.V., Fabian, K., Béguin, A., Kusters, M.E., Cortés-Ortuño, D., Fu, R.R., Jansen, C.M.L., Harrison, R.J., Leeuwen, T., and Barnhoorn, A., 2021, Micromagnetic Tomography for Paleomagnetism and Rock-Magnetism: *Journal of Geophysical Research: Solid Earth*, v. 126, doi:10.1029/2021JB022364.
- Heller, F., and Liu, T.-S., 1984, Magnetism of Chinese loess deposits: *Geophysical Journal International*, v. 77, p. 125–141, doi:10.1111/j.1365-246X.1984.tb01928.x.
- Heller, F., and Liu, T.-S., 1986, Palaeoclimatic and sedimentary history from magnetic susceptibility of loess in China: *Geophysical Research Letters*, v. 13, p. 1169–1172, doi:10.1029/GL013i011p01169.
- Hu, P., Liu, Q., Torrent, J., Barrón, V., and Jin, C., 2013, Characterizing and quantifying iron oxides in Chinese loess/paleosols: Implications for pedogenesis: *Earth and Planetary Science Letters*, v. 369–370, p. 271–283, doi:10.1016/j.epsl.2013.03.033.
- Kosmas, C.S., 1986, Relationship among Derivative Spectroscopy, Color, Crystallite Dimensions, and Al Substitution of Synthetic Goethites and Hematites 1: *Clays and Clay Minerals*, v. 34, p. 625–634, doi:10.1346/CCMN.1986.0340602.
- Kukla, G., Heller, F., Ming, L.X., Chun, X.T., Sheng, L.T., and Sheng, A.Z., 1988, Pleistocene climates in China dated by magnetic susceptibility: *Geology*, v. 16, p. 811, doi:10.1130/0091-7613(1988)016<0811:PCICDB>2.3.CO;2.
- Lima, E.A., and Weiss, B.P., 2016, Ultra-high sensitivity moment magnetometry of geological samples using magnetic microscopy: *Geochem. Geophys. Geosyst.*, v. 17, p. 3754–3774, doi:10.1002/2016GC006487.
- Liu, Q., Barrón, V., Torrent, J., Eeckhout, S.G., and Deng, C., 2008, Magnetism of intermediate hydromaghemite in the transformation of 2-line ferrihydrite into hematite and its paleoenvironmental implications: *Journal of Geophysical Research*, v. 113, p. B01103, doi:10.1029/2007JB005207.
- Liu, Q.S., Torrent, J., Barrón, V., Duan, Z.Q., and Bloemendal, J., 2011, Quantification of hematite from the visible diffuse reflectance spectrum: effects of aluminium substitution and grain morphology: *Clay Minerals*, v. 46, p. 137–147, doi:10.1180/claymin.2011.046.1.137.
- Maher, B.A., 1998, Magnetic properties of modern soils and Quaternary loessic paleosols: paleoclimatic implications: *Palaeogeography, Palaeoclimatology, Palaeoecology*, v. 137, p. 25–54, doi:10.1016/S0031-0182(97)00103-X.

- Maher, B.A., 1988, Magnetic properties of some synthetic sub-micron magnetites: *Geophys. J.*, v. 94, p. 83–96.
- Maher, B.A., 2016, Palaeoclimatic records of the loess/palaeosol sequences of the Chinese Loess Plateau: *Quaternary Science Reviews*, v. 154, p. 23–84, doi:10.1016/j.quascirev.2016.08.004.
- Maher, B.A., Alekseev, A., and Alekseeva, T., 2003, Magnetic mineralogy of soils across the Russian Steppe: climatic dependence of pedogenic magnetite formation: *Palaeogeography, Palaeoclimatology, Palaeoecology*, v. 201, p. 321–341, doi:10.1016/S0031-0182(03)00618-7.
- Maher, B.A., Mutch, T.J., and Cunningham, D., 2009, Magnetic and geochemical characteristics of Gobi Desert surface sediments: Implications for provenance of the Chinese Loess Plateau: *Geology*, v. 37, p. 279–282.
- Maher, B.A., and Possolo, A., 2013, Statistical models for use of palaeosol magnetic properties as proxies of palaeorainfall: *Global and Planetary Change*, v. 111, p. 280–287.
- Maher Taylor, R., 1988, . Formation of ultrafine-grained magnetite in soils. *Nature*, Vol. 336, p. 368-370.:
- Maher, B.A., and Thompson, R., 1991, Mineral magnetic record of the Chinese loess and paleosols: *Geology*, v. 19, p. 3, doi:10.1130/0091-7613(1991)019<0003:MMROTC>2.3.CO;2.
- Maher, B.A., and Thompson, R., 1992, Paleoclimatic Significance of the Mineral Magnetic Record of the Chinese Loess and Paleosols: *Quaternary Res.*, v. 37, p. 155–170, doi:10.1016/0033-5894(92)90079-X.
- Maher, B.A., Thompson, R., and Zhou, L.P., 1994, Spatial and temporal reconstructions of changes in the Asian palaeomonsoon: A new mineral magnetic approach: *Earth Planet. Sci. Lett.*, v. 125, p. 461–471.
- Maxbauer, D.P., Feinberg, J.M., and Fox, D.L., 2016, Magnetic mineral assemblages in soils and paleosols as the basis for paleoprecipitation proxies: A review of magnetic methods and challenges: *Earth-Science Reviews*, v. 155, p. 28–48, doi:10.1016/j.earscirev.2016.01.014.
- Maxwell, R.E., and Garrick-Bethell, I., 2020, Evidence for an Ancient Near-Equatorial Lunar Dipole From Higher Precision Inversions of Crustal Magnetization: *Journal of Geophysical Research: Planets*, v. 125, doi:10.1029/2020JE006567.
- McGee, D., 2020, Glacial–Interglacial Precipitation Changes: *Annual Review of Marine Science*, v. 12, p. 525–557, doi:10.1146/annurev-marine-010419-010859.

- Nie, J., King, J.W., and Fang, X., 2008, Link between benthic oxygen isotopes and magnetic susceptibility in the red-clay sequence on the Chinese Loess Plateau: *Geophysical Research Letters*, v. 35, p. L03703, doi:10.1029/2007GL032817.
- Nie, J., Song, Y., King, J.W., and Egli, R., 2010, Consistent grain size distribution of pedogenic maghemite of surface soils and Miocene loessic soils on the Chinese Loess Plateau: *ROCK MAGNETISM, SURFACE SOILS AND MIOCENE LOESSIC SOILS: Journal of Quaternary Science*, v. 25, p. 261–266, doi:10.1002/jqs.1304.
- Orgeira, M.J., Egli, R., and Compagnucci, R., 2011, A quantitative model of magnetic enhancement in loessic soils, *in The Earth's Magnetic Interior*, Dordrecht, Springer, p. 361–397.
- Roberts, A.P., Almeida, T.P., Church, N.S., Harrison, R.J., Heslop, D., Li, Y., Li, J., Muxworthy, A.R., Williams, W., and Zhao, X., 2017, Resolving the Origin of Pseudo-Single Domain Magnetic Behavior: *Journal of Geophysical Research: Solid Earth*, v. 122, p. 9534–9558, doi:10.1002/2017JB014860.
- Sharifigarmdareh, J., Khormali, F., Scheidt, S., Rolf, C., Kehl, M., and Frechen, M., 2020, Investigating soil magnetic properties with pedogenic variation along a precipitation gradient in loess-derived soils of the Golestan province, northern Iran: *Quaternary International*, v. 552, p. 100–110, doi:10.1016/j.quaint.2019.11.022.
- Shepherd, T.G., 2014, Atmospheric circulation as a source of uncertainty in climate change projections: *Nature Geosci.*, v. 7, p. 703–708.
- Sun, Y., Clemens, S.C., An, Z., and Yu, Z., 2006, Astronomical timescale and palaeoclimatic implication of stacked 3.6-Myr monsoon records from the Chinese Loess Plateau: *Quaternary Science Reviews*, v. 25, p. 33–48, doi:10.1016/j.quascirev.2005.07.005.
- Taylor, R.M., Maher, B.A., and Self, P.G., 1986, Magnetite in soils: I. The synthesis of single-domain and superparamagnetic magnetite: *Clay Minerals*, v. 22, p. 411–422, doi:10.1180/claymin.1987.022.4.05.
- Torrent, J., Barrón, V., and Liu, Q., 2006, Magnetic enhancement is linked to and precedes hematite formation in aerobic soil: *Geophysical Research Letters*, v. 33, p. L02401, doi:10.1029/2005GL024818.
- Torrent, J., Liu, Q., Bloemendal, J., and Barrón, V., 2007, Magnetic Enhancement and Iron Oxides in the Upper Luochuan Loess-Paleosol Sequence, Chinese Loess Plateau: *Soil Science Society of America Journal*, v. 71, p. 1570–1578, doi:10.2136/sssaj2006.0328.
- Újvári, G., Kok, J.F., Varga, G., and Kovács, J., 2016, The physics of wind-blown loess: Implications for grain size proxy interpretations in Quaternary paleoclimate studies: *Earth-Science Reviews*, v. 154, p. 247–278, doi:10.1016/j.earscirev.2016.01.006.
- Vandenbergh, J., Zhisheng, A., Nugteren, G., Huayu, L., and Van Huissteden, K., 1997, New absolute time scale for the Quaternary climate in the Chinese Loess region by grain-size

analysis: *Geology*, v. 25, p. 35, doi:10.1130/0091-7613(1997)025<0035:NATSFT>2.3.CO;2.

- Volk, M.W.R., Fu, R.R., Trubko, R., Kehayias, P., Glenn, D.R., and Lima, E.A., 2022, QDMLab: A MATLAB toolbox for analyzing quantum diamond microscope (QDM) magnetic field maps.: *Comput. Geosci.*, v. 167, p. 105198.
- Xiao, G., Zong, K., Li, G., Hu, Z., Dupont-Nivet, G., Peng, S., and Zhang, K., 2012, Spatial and glacial-interglacial variations in provenance of the Chinese Loess Plateau: *Geophys. Res. Lett.*, v. 39, p. L20715.
- Yang, T., Hyodo, M., Zhang, S., Maeda, M., Yang, Z., Wu, H., and Li, H., 2013, New insights into magnetic enhancement mechanism in Chinese paleosols: *Palaeogeog. Palaeoclimatol. Palaeoecol.*, v. 369, p. 493–500, doi:10.1016/j.palaeo.2012.11.016.
- Yu, Y., 2010, Paleointensity determination using anhysteretic remanence and saturation isothermal remanence: *Geochem. Geophys. Geosyst.*, v. 11, p. Q02Z12, doi:10.1029/2009GC002804.
- Zhang, H., Nie, J., Liu, X., Pullen, A., Li, G., Peng, W., and Zhang, H., 2021, Spatially variable provenance of the Chinese Loess Plateau: *Geology*, v. 49.

**Pinpointing the mechanism of magnetic enhancement in modern soils using high-resolution magnetic field imaging**

Roger R. Fu<sup>1</sup>, Barbara A. Maher<sup>2</sup>, Junsheng Nie<sup>3</sup>, Peng Gao<sup>3</sup>, Thomas Berndt<sup>4</sup>, Elizabeth Folsom<sup>1</sup>, Timothy Cavanaugh<sup>5</sup>

<sup>1</sup>Department of Earth and Planetary Sciences, Harvard University, Cambridge, Massachusetts, USA.

<sup>2</sup>Centre for Environmental Magnetism and Palaeomagnetism, Lancaster Environment Centre, University of Lancaster, Lancaster, United Kingdom

<sup>3</sup>Key Laboratory of Western China's Environment System (Ministry of Education), College of Earth and Environmental Sciences, Lanzhou University, Lanzhou, China

<sup>4</sup>Department of Geophysics, School of Earth and Space Sciences, Peking University, Beijing, China

<sup>5</sup>Center for Nanoscale Systems, Harvard University, Cambridge, Massachusetts, USA.

**Contents of this file**

Text S1

Figures S1

**Introduction**

This Supporting Information file contains text describing the methodology for estimating grain size from ARM acquisition precision and a corresponding figure.

## S1. Application of thermoremanent magnetization (TRM) statistical recording limit analysis to anhysteretic remanent magnetization (ARM)

All natural forms of remanent magnetization except for lightning result in only a weak bias of magnetic grain magnetizations towards the ambient magnetic field direction. As a result, a substantial number of independent ferromagnetic grains is necessary to reveal a statistically significant bias. Even more grains are required to quantify the strength and direction of the ambient field with high precision. Berndt et al. (2016) quantified the relationship between the number of ferromagnetic grains and the precision of paleomagnetic recording, represented by the variance in direction and magnitude of the resulting magnetization, assuming a TRM acquisition process on single domain grains. Under these assumptions, the equilibrium probability,  $p$ , of a single grain being magnetized in the direction of the bias field is (Eq. 4-5 in Berndt et al. 2016):

$$p(\phi) = \frac{1}{2} [1 + \tanh(x_b \cos \phi)] \quad (1)$$

where  $\phi$  is the angle between the ambient field and the grain easy axis and  $x_b$  describes the balance between magnetic alignment energy and randomizing thermal energy:

$$x_b = \frac{\mu_0 V M_s B_0}{k T_B} \quad (2)$$

where  $\mu_0$ ,  $V$ ,  $M_s$ ,  $B_0$ ,  $k$ , and  $T_B$  are the permeability of free space, grain volume, saturation magnetization at time of grain blocking, ambient field strength, the Boltzmann constant, and the blocking temperature, respectively.

The analysis of Berndt et al. (2016) was derived for thermal, viscous, and chemical remanent magnetizations (TRM, VRM, CRM) only. In these processes, the magnetic remanence carriers reach a thermodynamic equilibrium just before blocking. To relate ARM precision to the number of remanence-carrying grains, the ARM, too, needs to be dominated by particles that reach a thermodynamic equilibrium (Eq. 1) upon remanence acquisition. This is satisfied only if sufficient opportunities are available to each grain for thermally activated processes, described by the energy balance of Eq. 2, to modify the grain magnetization. In TRM, VRM, and CRMs this is always the case since before blocking, magnetic grains are free to change their magnetic moment due to thermally activations. For ARMs, however, due to the applied strong AF field, particles can generally only change their magnetization in one direction: i.e., align with the AF field direction at each time. The frequency of thermally activated grain realignment following classic single domain Néel theory for uniaxial anisotropy is (Dunlop and Ozdemir, 1997, Eq. 8.3):

$$f(B) = f_0 \exp \left[ -\frac{B_k M_s V}{kT} \left( 1 - \frac{B}{B_k} \right)^2 \right] \quad (3)$$

where  $B_k$  is the microscopic coercivity,  $B$  is the ambient field, and  $T$  is the ambient temperature, which is room temperature for ARM experiments. The factor  $f_0 \approx 10^9 \text{ s}^{-1}$  represents the frequency with which thermal fluctuations result in opportunities to remagnetize the grain and  $f$  is the frequency at which such remagnetizations actually occur. For TRM, VRM, and CRMs, the field  $B$  is the weak (geomagnetic) ambient field; for ARMs, however,

$$B = B_{pulse} + B_0 \approx B_{pulse} \quad (4)$$

is the sum of the field strength of a single AF pulse  $B_{pulse}$  and the ARM bias field  $B_0$ , the latter of which is negligible compared to the former. For example, in our experiments a bias field of  $B_0 = 300 \text{ } \mu\text{T}$  was used while the AF field may have been  $B_{pulse} = 10 \text{ mT}$  for a given AF pulse during a single ARM acquisition. Since in our experiments the AF frequency is 613 Hz, a single pulse would have lasted for  $\tau = 816 \text{ } \mu\text{s}$ . For the duration of this pulse, all particles with a coercivity  $B_k$  below  $B_{pulse}$  align with the field; particles with a coercivity above  $B_{pulse}$  may also align with the field due to thermal activations. No particle, however, can anti-align with the field, during this pulse, however, preventing full thermal equilibrium from being reached during a single pulse.

Rearranging eq. (3), one can interpret the ratio  $f/f_0$  as the probability that the grain is remagnetized in a single ( $10^{-9} \text{ s}$  duration) thermal fluctuation. The probability that a grain is not remagnetized during a single thermal fluctuation is therefore  $1 - f(B_{pulse})/f_0$ , and the probability that a grain is not remagnetized at least once during a single AF pulse of amplitude  $B_{pulse}$  and duration  $\tau$  is therefore

$$p(B_{pulse}) = 1 - \left( 1 - f(B_{pulse})/f_0 \right)^{\tau f_0} \quad (5)$$

where the product  $\tau f_0$  can be seen as the number of “thermal activation attempts” during a single AF pulse duration.

When the applied field is equal to or greater than  $B_k$ , the probability of remagnetization towards the bias field direction during each pulse (or indeed each thermal fluctuation) is 1, corresponding to deterministic remagnetization of the grain towards the applied field direction and making the field application equivalent to an isothermal remanent magnetization (IRM). As a result, upon all AF pulse applications  $\geq B_k$ , the magnetization of the grain is not in thermal equilibrium and the statistical reliability/scatter of the direction cannot be used to assess the number of particles.

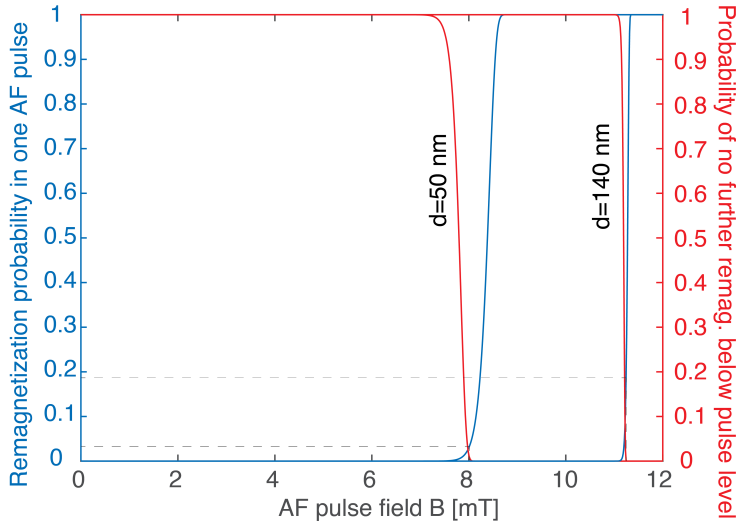


**Figure S1.** Predicted behavior of magnetite particles upon AF or ARM application. Blue curves indicate the probability of field-assisted thermal remagnetization of a grain with the given diameter during a single AF pulse. Red curves denote the probability that the grain would undergo no further remagnetizations during the AF ramp down after a given AF pulse field level. Dashed gray lines indicate the single-pulse remagnetization probability of a grain that has 99% probability of being remagnetized during the remaining AF ramp down. A low value indicated by the gray line implies that the grain is more likely to reach thermal equilibrium. Assumed grain sizes and  $B_k = 12$  mT correspond to the ultrafine magnetite population found in the high precipitation soil. See text for details and additional parameters.

Probabilistic, thermally-assisted remagnetization of the grain according to Eq. 3 may occur during the AF pulses after the field value falls below  $B_k$ . In these cases, the grain under a 0 K environment would not be remagnetized, but at laboratory conditions may be remagnetized due to a combination of thermal energy and the pulse field decreasing the energy barrier according to Eq. 3. For AF pulses slightly smaller than  $B_k$ , the probability of remagnetization during each pulse remains high, implying that the resulting grain magnetizations are still mostly deterministic (see blue curves in Fig. S1). Conversely, for the pulses where  $B_{pulse}$  is significantly smaller than  $B_k$ , the outcome becomes less deterministic and the distribution of grain magnetization would converge towards the thermal equilibrium of  $B_0$  in Eqs. 1-2 after infinitely many pulse applications.

Naturally, for very weak AF fields  $B_{pulse}$ , the probability of a thermally activated change in magnetization for a particle approaches zero. It would therefore take an infinitely long time and require infinitely many pulses to reach thermal equilibrium. There is, however, an intermediate range where the probability that a particle is remagnetized during one pulse is significantly smaller than 1, yet large enough such that

repeated application of AF pulses will reach a thermal equilibrium. For example, if the probability of remagnetization during one pulse is 1%, then the application of 500 repeated pulses leads to a total probability of remagnetization of  $(1 - 0.01)^{500} = 99\%$ , achieving virtually thermal equilibrium.

One needs to keep in mind, however, that the AF field is continuously being ramped down. Hence, any given grain can only reach thermodynamic equilibrium due to repeated application of successively lower fields. The probability of a grain avoiding remagnetization (i.e., failing to reach thermodynamic equilibrium) after the AF ramped down to zero from a given value  $B_{pulse}$  can be computed as the product of the grain avoiding remagnetization at each pulse at and below  $B_{pulse}$  (Eq. 5; red curves in Fig. S1).

In summary, two conditions need to be fulfilled for a grain to reach thermodynamic equilibrium. First, it needs to have a high probability of being remagnetized at some point during successive AF pulse applications after  $B_{pulse}$  drops well below its microscopic coercivity  $B_k$ . Second, the grain must simultaneously have a low probability  $p(B_{pulse})$  of being remagnetized during a single AF pulse, since this would otherwise be a deterministic process akin to an IRM. Having these two conditions fulfilled implies that the grain is highly likely to be remagnetized at least once under conditions where the effect of the AF pulse field is non-deterministic and the probability of remagnetization is guided by the balance of magnetic and thermal energies.

Therefore, applying a large number of AF pulses each representing a small probability of thermally remagnetizing the grain can result in a final grain magnetization distribution close to thermal equilibrium. To do so, we apply an AF ramp with very slow decay in peak pulse field strengths. We find that, for our AF frequency of 613 Hz, a ramp down rate of  $1 \text{ mT s}^{-1}$  results in 99% of 50-140 nm grains being remagnetized after the per-pulse probability of remagnetization has declined to less than 0.2 (Fig. S1). This implies that these ramp parameters are sufficient for magnetite grains associated with the ultrafine ferrimagnetic population to approximate thermal equilibrium, thereby validating the use of recording limit results for TRM on our ARM acquisition data.

## References:

- Berndt, T., Muxworthy, A.R., and Fabian, K., 2016, Does size matter? Statistical limits of paleomagnetic field reconstruction from small rock specimens: *J. Geophys. Res. Solid Earth*, v. 121, p. 15–26, doi:10.1002/2015JB012441.
- Dunlop, D.J., and Ozdemir, O., 1997, *Rock Magnetism: Fundamentals and Frontiers*: New York, Cambridge University Press, Cambridge Studies in Magnetism, 573 p.